Defects tune the acidic strength of amorphous aluminosilicates

Rishi Verma [1], Charvi Singhvi [1], Amrit Venkatesh [2] & Vivek Polshettiwar [1]

Crystalline zeolites have high acidity but limited utility due to microporosity, whereas mesoporous amorphous aluminosilicates offer better porosity but lack sufficient acidity. In this work, we investigated defect engineering to fine-tune the acidity of amorphous acidic aluminosilicates (AAS). Here we introduced oxygen vacancies in AAS to synthesize defective acidic aluminosilicates (D-AAS). ^{1}H, ^{27}Al, and ^{17}O solid-state nuclear magnetic resonance (NMR) studies indicated that defects induced localized structural changes around the acidic sites, thereby modifying their acidity. X-ray photoelectron spectroscopy (XPS) and Fourier transform infrared (FTIR) spectroscopy studies substantiated that oxygen vacancies alter the chemical environment of Brønsted acidic sites of AAS. The effect of defect creation in AAS on its acidity and catalytic behavior was demonstrated using four different acid-catalyzed reactions namely, styrene oxide ring opening, vesidryl synthesis, Friedel-Crafts alkylation, and jasminaldehyde synthesis. The defects played a role in activating reactants during AAS-catalyzed reactions, enhancing the overall catalytic process. This was supported by in-situ FTIR, which provided insights into the molecular-level reaction mechanism and the role of defects in reactant activation. This study demonstrates defect engineering as a promising approach to fine-tune acidity in amorphous aluminosilicates, bridging the porosity and acidity gaps between mesoporous amorphous aluminosilicates and crystalline zeolites.

In the realm of heterogeneous catalysis, the quest for materials that combine superior porosity with substantial acidity has been a long-standing challenge. Crystalline zeolites are renowned for their exceptional acidity, yet their practical utility is often limited by their inherent microporosity, which restricts access to active sites and hampers the diffusion of reactants[1–4]. Conversely, mesoporous amorphous aluminosilicates offer enhanced porosity and accessibility, yet they typically lack the level of acidity found in their crystalline counterparts[5–10]. Addressing this dichotomy and seeking a viable solution to bridge the gap between porosity and acidity represents a fundamental pursuit in catalytic materials research[11–28].

The acidity can be fine-tuned through factors such as the chemical composition involving framework and extra-framework species, as well as the synthesis and pretreatment procedures. Defects have long been employed as a means to fine-tune the catalytic behavior of materials[29–42], yet their potential for precisely modulating acidity in solid acids has remained relatively unexplored. Building upon our ongoing research into defect-tuned catalysis[43–45], using dendritic fibrous nanosilica (DFNS)-based catalysts[46–51], in this study, we introduce an approach that utilizes defect tuning as a strategic tool for customizing the acidity of solid acids.

This study hypothesizes that manipulating defects holds promise as an effective method for refining the acidity of amorphous aluminosilicates, effectively bridging the existing disparities in porosity and acidity between mesoporous amorphous aluminosilicates and crystalline zeolites.

^{1}Department of Chemical Sciences, Tata Institute of Fundamental Research (TIFR), Mumbai 400005, India. ^{2}National High Magnetic Field Laboratory, Florida State University, Tallahassee, FL 32310, USA. ✉e-mail: avenkatesh@magnet.fsu.edu; vivekpol@tifr.res.in

Results and discussion

To investigate our hypothesis, we employed nanosponges of 'acidic aluminosilicates' (AAS)[47]. We then artificially introduced and controlled the oxygen vacancy sites in AAS using the magnesiothermic[43] protocol to synthesize defective acidic aluminosilicates (D-AAS). Our investigation incorporated a range of analytical techniques to shed light on the impact of defects on the material's acidity. Solid-state nuclear magnetic resonance (NMR) studies revealed localized structural changes surrounding the acidic sites, thereby altering their acidic properties. X-ray photoelectron spectroscopy (XPS) and Fourier-transform infrared (FTIR) spectroscopy analyses further affirmed that the presence of oxygen vacancies induced changes in the chemical environment of Brønsted acidic sites in AAS, leading to an overall enhancement in acidity. Complementary assessments, including oxygen storage capacity and ammonia temperature-programmed desorption (TPD) studies, established a valuable correlation between defect concentration and catalyst acidity.

We then assessed the practical implications of defect creation in AAS by investigating its effects across four distinct acid-catalyzed reactions: styrene oxide ring opening, vesidryl synthesis, Friedel–Crafts alkylation, and jasminaldehyde synthesis. These examinations illuminated the role of defects in catalytic processes by facilitating reactant activation within AAS, thereby contributing to an overall improvement in catalytic efficiency. Furthermore, our in-situ FTIR studies provided valuable insights into the molecular-level reaction mechanism, elucidating the pivotal role played by defects in reactant activation.

Synthesis and characterization of AAS and D-AAS

AAS was synthesized by achieving an efficient hetero-condensation between tetraethylorthosilicate (TEOS) and aluminum acetylacetonate (Al(acac)$_3$) precursors having comparable hydrolysis rates to avoid homo-condensation and the formation of two distinct phases (Supplementary Fig. 1)[47]. Defects were generated by treating AAS with magnesium (Mg) at 650 °C under argon flow (100 mL min^{-1}), followed by acid washing to remove the unreacted Mg and Mg species (Supplementary Fig. 2)[43]. Using two different Mg amounts, D-AAS-12 (12 wt% Mg) and D-AAS-25 (25 wt% Mg), the concentration of defects in AAS was tuned.

Scanning electron microscopy (SEM) analysis of AAS revealed the formation of a porous nanosponge morphology (Fig. 1a), which remained intact even after defect formation, in D-AAS-12 and D-AAS-25 (Fig. 1b, c). Transmission electron microscopy (TEM) images of AAS, D-AAS-12, and D-AAS-25 further confirmed the presence of the nanosponge morphology (Fig. 1d–f). The energy-dispersive X-ray spectroscopy (EDS) elemental composition of both AAS and D-AAS (Supplementary Table 1), indicated the Si/Al ratio of 2.13 in AAS, while this ratio increases to 2.88 in D-AAS-12 and further to 3.75 in D-AAS-25 (3.75) (Supplementary Table 1). We did not observe any magnesium content in the SEM-EDS indicating the efficient removal of all the Mg species from the D-AAS sample during the washing step (Supplementary Table 1). This was further confirmed by quantifying the metal content by inductively coupled plasma mass spectrometry (ICP-MS, Supplementary Table 1). These observations indicated that the treatment of AAS with magnesium at 650 °C not only led to the removal of oxygen atoms from the AAS network but also reacted and removed some of the Al sites during the acid-washing step of defect creation. To investigate if there was any phase separation during defect creation, scanning transmission electron microscopy-energy-dispersive X-ray spectroscopy (STEM-EDS) elemental mapping was used, which revealed a uniform distribution of Si, Al, and O across all samples of AAS, D-AAS-12, and D-AAS-25 (Supplementary Fig. 3), indicating no phase separation, which was further confirmed by powder X-ray diffraction (PXRD) (Supplementary Fig. 4).

The surface area showed a decreasing trend from $525 \pm 25\ \mathrm{m^2\ g^{-1}}$ in AAS to $485 \pm 18\ \mathrm{m^2\ g^{-1}}$ in D-AAS-12 and further to $473 \pm 24\ \mathrm{m^2\ g^{-1}}$ in D-AAS-25 (Fig. 1g–i). This decline was attributed to some loss in the nanosponge structure, with an increase in the magnesium amount during defect creation. Furthermore, the pore size distribution analysis revealed broader pore size distributions in the case of D-AAS-12 and D-AAS-25 compared to AAS (Fig. 1j–l). This observation suggests that during defect creation, the structure of AAS was altered and caused the rupture of some pore walls, leading to larger pore diameters in D-AAS-12 and D-AAS-25.

Defect creation in AAS resulted in the formation of radical centers, which tend to absorb light of different wavelengths[45,52]. The color of AAS transformed from white to light brown in D-AAS-12 and finally to dark brown in D-AAS-25 (inset of Fig. 1a–c). The ultraviolet-visible diffuse reflectance spectroscopy (UV–Vis–DRS) spectra of D-AAS-12 and D-AAS-25 exhibited an increase in absorbance within the broad-band range of 250–550 nm as compared to AAS (Supplementary Fig. 5a). AAS displayed a minimal absorbance, possibly attributed to the presence of naturally occurring defects during the synthesis process[53–55]. With an increase in the magnesium content, a greater number of defects were generated, ultimately leading to elevated absorbance levels and alterations in the color of D-AAS-12 and D-AAS-25 (Supplementary Fig. 5a). The convoluted nature of the absorption spectra makes it difficult to separate and distinguish between different absorption bands. However, the broad absorbance spectrum could provide some insights into the existence of different light absorption sites. The absorption across various wavelengths may originate from distinct sources, such as non-bridging oxygen hole centers (NBOHC) (Si–O•) sites at approximately 261 and 290 nm, bulk peroxy radicals at 378 nm, and broadband at 434 nm indicative of silicon-associated hole centers[43,54,55]. All the absorption bands in the spectra were broad and poorly resolved, hence the deconvolution of these overlapping bands was challenging. The broadness observed in the absorption spectra stemmed from variations in the local defect environment within the material due to the material's amorphous nature. This non-equivalence from site to site resulted in variations in optical transition energies and the inhomogeneous broadening of the spectra[54,55].

In a photoluminescence (PL) study, when the AASs were irradiated with 400 nm light, a prominent and broad luminescence spanning the range of 760–800 nm, with a peak showing maximum luminescence at 795 nm, was observed (Supplementary Fig. 5b). This significant PL band was ascribed to electronic transitions taking place at the NBOHC sites[56,57]. The broadening of the photoluminescence emission spectra, akin to the UV–Vis–DRS absorption spectra, can be attributed to the heterogeneous nature of the surrounding environment encompassing NBOHCs, a consequence of the amorphous characteristics exhibited by AAS and its defective counterparts. The intensity of the PL emission exhibited an increment from AAS to D-AAS-12 (1.5 times) and further to D-AAS-25 (2.1 times), indicative of an increase in the concentration of defect sites with the increasing magnesium amount.

Comprehensive molecular insights into defect sites through solid-state NMR analysis

Solid-state NMR spectroscopy has been shown to be a useful tool for the characterization of aluminosilicate materials[7]. To probe the local structural changes in AAS after defect creation, we utilized high-field (18.8 T) solid-state NMR spectroscopy (Fig. 2). The ^{1}H solid-state NMR spectrum of AAS showed signals characteristic of aluminosilicates including bridging hydroxyl groups (SiOHAl) around 4.7 ppm[11], silanol (SiOH), and pseudo-bridging silanol groups (SiOH---Al) at 1.2 and 1.9 ppm, respectively (Fig. 2a, f)[11,58–62]. Differences in ^{1}H chemical shifts of free bridging hydroxyl groups (3.6–4.3 ppm) and those that are hydrogen-bonded to neighboring oxygen atoms (4.6–5.2) have also been noted previously (Fig. 2a, f)[11,63]. The signal around 6.9 ppm was previously assigned to water adsorbed on Lewis acid sites (Fig. 2a, f)[58].
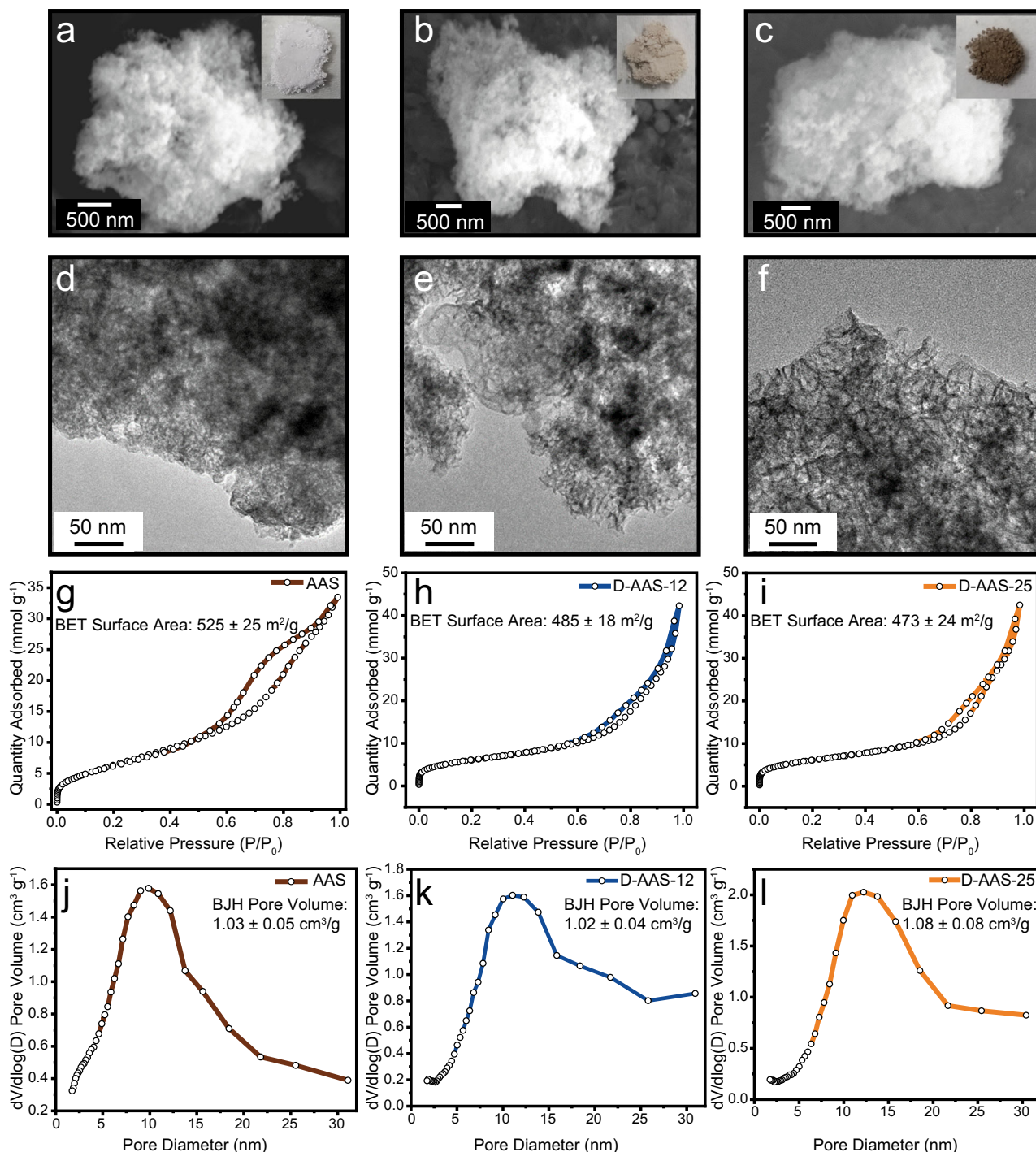
Fig. 1 | Structural and surface characterization of AAS and defective AAS. SEM and TEM images of **a**, **d** AAS, **b**, **e** D-AAS-12, and **c**, **f** D-AAS-25. Inset: optical images; Nitrogen sorption isotherms of **g** AAS, **h** D-AAS-12, and **i** D-AAS-25, Brunauer–Emmett–Teller (BET) surface areas are written in the plots; Barrett–Joyner–Halenda (BJH) adsorption pore-size distributions of **j** AAS, **k** D-AAS–12, and **l** D-AAS-25. Error bars: Standard deviation calculated from data of at least three repeated experiments.

Upon inducing defects in AAS, changes were observed in the 1D ^{1}H NMR spectrum of D-AAS-12: heightened relative signal intensities at 3.9 and 1.3 ppm were observed relative to signals at 4.7 and 1.9 ppm, respectively (Fig. 2a). The increase in the 1.3 ppm signal intensity can be ascribed to the creation of oxygen vacancies in AAS, causing the rupture of some Si–O–Al bonds. Subsequent acid washing leads to the hydrolysis of these vacant sites, generating an increased population of Si–OH species. Furthermore, the heightened intensity at 3.9 ppm may be attributed to a relative increase in free bridging hydroxyl groups (3.9 ppm) in comparison to hydrogen-bonded bridging hydroxyl groups (Fig. 2a). This observation is consistent with a reduction in hydrogen bond interactions between bridging hydroxyl groups and neighboring hydroxyl groups, as oxygen vacancies were introduced.

^{27}Al solid-state NMR spectra provided valuable insights into the Al coordination environments within the framework. Three characteristic peaks were observed at ca. 2, 30, and 55 ppm, corresponding to 6-, 5- and 4-coordinate Al sites, respectively (Supplementary Fig. 6)[11,47,58–64]. When defects were introduced, a noticeable alteration in the relative
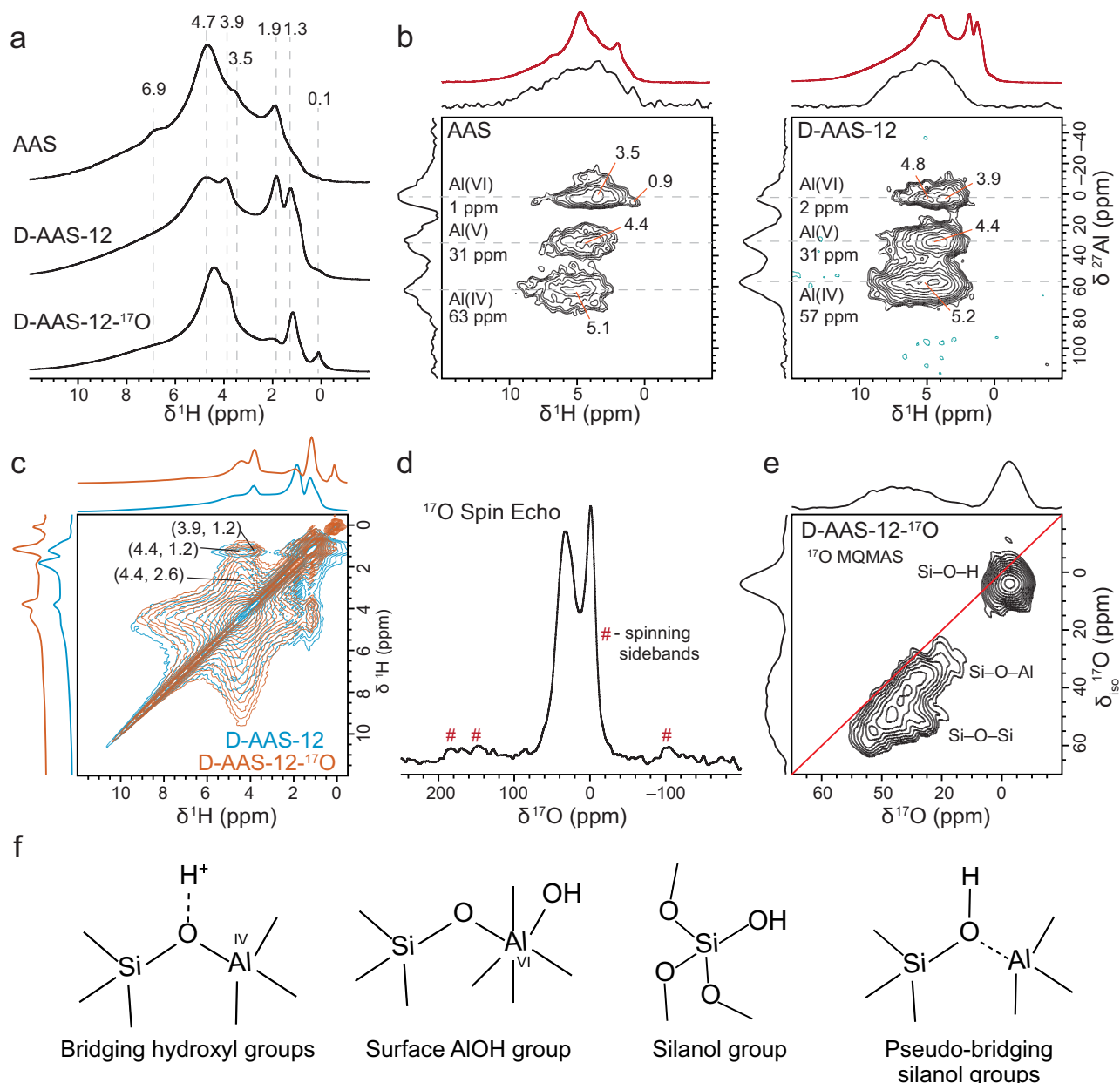
Fig. 2 | Structural analysis by solid-state NMR of AAS and defective AAS. Solid-state NMR spectra of AAS, D-AAS-12, and D-AAS-12-^{17}O. **a** 1D ^{1}H MAS spectra of AAS, D-AAS-12, and D-AAS-12-^{17}O. **b** 2D ^{27}Al → ^{1}H D-RINEPT spectra of AAS and D-AAS-12. **c** Overlay of 2D ^{1}H–^{1}H spin diffusion spectra of D-AAS-12 (blue) and D-AAS-12-^{17}O (orange) acquired with a 50 ms spin diffusion time. **d** 1D ^{17}O solid-state NMR spectrum. **e** 2D ^{17}O multiple quantum magic angle spinning (MQMAS) spectrum of D-AAS-12-^{17}O. Spinning sidebands in the 1D ^{17}O NMR spectrum are indicated. The shoulder at ca. 60 ppm likely arises from satellite transitions. In the MQMAS spectrum, the F_1 dimension shows the isotropic quadrupolar frequency (δ_{iso}) obtained after shearing. **f** Structures of various sites present in AAS and D-AAS.

peak intensities was observed, primarily involving a decrease in the intensity of Al(VI) from 18% in AAS to 13% in D-AAS-12, indicating the breaking of some Al−O bonds (Supplementary Figs. 6, 7, Supplementary Table 2). Assuming a similar amount of sample in all the rotors to within 5–10% by mass, a comparison of the absolute ^{27}Al integrated signal intensities shows a ca. 10% and 40% reduction in intensity with D-AAS-12 and D-AAS-25, respectively, in comparison to AAS. These NMR observations are consistent with SEM-EDS results which show a 16% and 30% reduction in Al content with D-AAS-12 and D-AAS-25 (Supplementary Table 1). Furthermore, since the defect generation results in radical formation (see below), some fraction of the ^{27}Al NMR signals may be invisible due to paramagnetic signal quenching. This effect will be exacerbated for D-AAS-25, where there is a higher radical concentration. The reduction in Al content appears to occur across Al(VI),

Al(V), and Al(IV) sites in D-AAS-25, resulting in a similar amount of Al(IV) in comparison to AAS (Supplementary Fig. 7). This observation could explain the similar acidity between AAS and D-AAS-25, while D-AAS-12, which contains the highest amount of Al(IV) sites, shows the highest acidity (described in subsequent sections).

Figure 2b shows 2D proton-detected ^{1}H–^{27}Al heteronuclear correlation spectra of AAS and D-AAS-12 obtained using the dipolar refocused insensitive nuclei enhanced by polarization transfer (D-RINEPT) pulse sequence[65,66]. Al(VI) Al(V), Al(IV) signals[11,47,58–64] were found to correlate with broad distributions of ^{1}H signals consistent with previous observations in amorphous aluminosilicates[11]. Evidently, a correlation between Al(VI) and the ^{1}H signal at 0.9 ppm was observed in the case of AAS, which likely corresponds to Al^{VI}−OH species, wherein aluminum is linked to six oxygen atoms−five of which form

Al–O–Si bonds, and one forms an Al–OH bond. This species was presumably attributed to surface terminal Al–OH groups in AAS. In contrast, such a correlation was absent in the case of D-AAS-12, potentially indicating the removal of octahedral Al–OH species. Furthermore, consistent with the quantitative 1D ^{27}Al spectra (Supplementary Figs. 6, 7), the relative intensity of Al(VI) with respect to Al(IV) decreased with D-AAS-12 compared to AAS, suggesting the disruption of Al–O bonds (Fig. 2b).

2D ^{1}H–^{1}H spin diffusion spectra of D-AAS-12 shown in Fig. 2c and Supplementary Fig. 8 highlight several cross peaks that indicate close spatial proximity between different sites: bridging SiOHAl and SiOH species (3.9 and 1.2 ppm, 4.4 and 1.2 ppm), and bridging SiOHAl and bridging AlOH groups (4.4 and 2.6 ppm)[11,63]. 2D ^{1}H–^{1}H single quantum (SQ)–double quantum (DQ) correlation spectrum of D-AAS-12 also shows strong auto-correlations for signals at 1.2 (SiOH), 3.9 (bridging SiOHAl) and 7 ppm (water), suggesting close proximity of similar species (Supplementary Fig. 9).

To elucidate the nature of defect sites using ^{17}O solid-state NMR spectroscopy and assess the influence of water adsorption, ^{17}O-labeled water (90%) was introduced to D-AAS-12 (D-AAS-12-^{17}O). A relative increase in the 4.4 ppm signal (hydrogen-bonded bridged hydroxyl groups) was observed in the ^{1}H solid-state NMR spectrum, indicating an expected increase in hydrogen bonding upon water addition. Moreover, the isolated terminal Al–OH signal at 0.1 ppm became more prominent, signifying enhanced hydrolysis in the presence of water. Simultaneously, the signal at 1.9 ppm broadened, suggesting hydrogen-bonding interactions of water molecules with pseudo-bridging silanols (Fig. 2a). This broadening results from diverse hydrogen bond interactions involving pseudo-bridging silanols with entities such as added water molecules, neighboring silanol groups, or neighboring Al–OH groups—all of which tend to increase upon addition of water. The dynamic behavior of water molecules also contributes to the broadening of the signal around 1.9 ppm.

Upon the addition of water, the ^{1}H–^{1}H spin diffusion spectra of D-AAS-12-^{17}O revealed cross peaks consistent with D-AAS-12, indicating that interactions between Si–OH–Al and SiOH/AlOH were still present after water adsorption on defect sites (Fig. 2c and Supplementary Fig. 8). Importantly, the ^{1}H–^{1}H spin diffusion spectra suggested that defect creation did not impact the overall textural properties of the material, and the introduction of water at defect centers did not hinder existing interactions.

The adsorption of water on the defect sites was directly confirmed using ^{27}Al and ^{17}O solid-state NMR spectroscopy. Upon the addition of water, the relative population of Al(IV) sites decreased with a concomitant increase in the population of Al(V) sites, while there was no observable increase in Al(VI) sites (Supplementary Figs. 6, 7). This observation could indicate that Al(IV) sites are more likely to react with the added water, resulting in hydrolyzed Al(V) species. This observation is also consistent with the hypothesized relationship between increased acidity and higher Al(IV) speciation in D-AAS-12.

^{17}O solid-state NMR could be a potentially valuable tool to probe the local environment of the defect sites introduced in AAS. However, ^{17}O has a low natural abundance of 0.037% and is a spin-5/2 quadrupolar nucleus, which results in poor NMR sensitivity and necessitates isotopic enrichment. ^{17}O labeling of zeolitic materials has seen renewed interest recently with the introduction of several isotopic enrichment strategies[67–70]. Morris, Ashbrook, and co-workers recently showed that a uniform ^{17}O enrichment of zeolitic frameworks could be achieved by mixing dehydrated zeolites with H$_2$^{17}O at room temperature for a few days[69,71]. In the case of D-AAS-12, we expected a rapid ^{17}O enrichment due to the increased acidity of the material and the presence of oxygen vacancies. Indeed, stirring D-AAS-12 with 90% H$_2$^{17}O at room temperature for one hour, followed by removal of excess water at 120 °C produces a uniform enrichment across Si–OH, Si–O–Si, and Si–O–Al sites (Fig. 2d and e) (detailed synthetic procedures are described in the experimental section). A 1D ^{17}O spin echo spectrum of D-AAS-12-^{17}O labeled using this approach could be rapidly acquired within 2.5 min (Fig. 2d). The resolution of the ^{17}O solid-state NMR spectrum was substantially improved by obtaining a multiple quantum magic angle spinning (MQMAS)[72,73] spectra which required only 6.5 h of acquisition time (Fig. 2e). Signals characteristic of Si–OH, Si–O–Si, and Si–O–Al was observed, indicating the uniform adsorption of H$_2$^{17}O at these sites[69,70,74,75]. The high sensitivity with which these ^{17}O solid-state NMR spectra were obtained validates the high efficiency of the ^{17}O labeling approach used here. These results support the idea that ^{17}O-labeling of D-AAS-12 is likely accelerated by its increased acidity and the presence of oxygen vacancies, facilitating acid hydrolysis. A more detailed characterization of the oxygen environments in these materials will be the subject of future work.

Characterization of AAS and D-AAS

To obtain deeper insights into the characteristics of defects, an XPS analysis was conducted (Supplementary Fig. 10). The XPS analysis of the Si 2p region revealed two distinct peaks at 103.2 and 103.9 eV, which were attributed to the presence of Si atoms in Si–O–Si or Si–O–Al bonds, as well as silanol groups[43,76,77]. Upon the introduction of defect sites, additional peaks emerged in the spectra of D-AAS-12 and D-AAS-25 at 101.5 and 99.4 eV, and these peaks were assigned to the presence of NBOHC sites and elemental Si, respectively[43]. The peak area exhibited an increasing trend as the concentration of defects increased from D-AAS-12 to D-AAS-25 (Supplementary Fig. 10a, d, g). Additionally, when considering the relative area percentages, the peak area percentage corresponding to NBOHC increased from 2.1% in D-AAS-12 to 6.7% in D-AAS-25 (Supplementary Fig. 10d, g). Similar observations were made in the O 1s spectra of AAS, D-AAS-12, and D-AAS-25 (Supplementary Fig. 10b, e, h). The O 1s spectrum of AAS exhibited three peaks at 531.5, 532.5, and 533.5 eV, which were attributed to the O atom in NBOHC sites, the Si–O–Al network, and the hydroxyl group[43,76–80]. The peak at a higher binding energy of 533.5 eV could also arise from the presence of adsorbed water[76]. The relative area corresponding to NBOHC sites increased from AAS (11.3%) to D-AAS-12 (17.2%) and further to D-AAS-25 (23.2%), indicating a rise in the concentration of defect sites with increasing magnesium content (Supplementary Fig. 10b, e, h).

In the case of Al 2p XPS spectra of AAS, D-AAS-12, and D-AAS-25, the spectra were again de-convoluted into three peaks at 74.5, 75.5, and 76.5 eV, which were assigned to tetrahedral Al sites Al(IV), penta-coordinated Al sites Al(V), and octahedral Al(VI) sites, respectively (Supplementary Fig. 10c, f, i)[76–79]. With the increase in defect concentration, the relative area corresponding to Al(IV) sites increased from AAS to D-AAS-12 and further to D-AAS-25. Similarly, the relative area corresponding to Al(VI) decreased from AAS to D-AAS-12 and further to D-AAS-25. Taken together with the NMR results, the observations corroborated with the breaking of the Al–O bonds on the creation of defects in AAS.

The oxygen vacancies or defects generated by the magnetiothermia treatments are known to have unpaired electrons i.e., radical formation. We performed electron paramagnetic resonance (EPR) analysis of AAS, D-AAS-12, and D-AAS-25 to understand the nature of these radicals. In the case of AAS, we observed a small EPR signal at $g = 1.999$, which indicated the presence of some NBOHC sites (Supplementary Fig. 11)[43,53,81–85]. As the concentration of the defects increased in D-AAS-12 and further in D-AAS-25, the intensity of the EPR signal also increased, indicating the increase in the concentration of defects (Supplementary Fig. 11). In the case of D-AAS-12, the EPR signal became broader which indicated that not only the concentration but the type of the defects was also increased going from AAS to D-AAS-12[43,53,81–85]. Furthermore, line broadening due to dipolar couplings between electron spins and g-anisotropy cannot be ignored. Additionally, we noted a shift in the EPR signal with the increasing

concentration of defects in both D-AAS-12 and D-AAS-25 samples. This phenomenon suggested that as the defect concentration increased, there may be concurrent alterations in the chemical nature or the local environment of the defect sites, thus resulting in potential changes in the *g*-factor. However, comprehensively probing the intricacies of these changes in the local environment surrounding the defect sites would necessitate a more thorough and specialized EPR investigation and such an in-depth study lies beyond the scope of the current work. The concentration of these sites further increased in the case of D-AAS-25 (Supplementary Fig. 11).

The influence of oxygen vacancies on the thermal behavior of AAS and D-AAS

Thermogravimetric analysis (TGA) revealed a distinctive two-step weight loss pattern upon heating (Supplementary Fig. 12). The initial weight loss step occurred around 120 °C, corresponding to the desorption of adsorbed water molecules from the catalyst's surface[47]. The percentage loss of adsorbed water increased from AAS (2.6%) to D-AAS-12 (6.5%) and further to D-AAS-25 (7.7%) (Supplementary Fig. 12). This observation suggests that an increase in oxygen vacancies enhances the water adsorption capacity of the material. The oxygen atoms of water molecules exhibit a higher affinity towards the oxygen vacancies present in D-AAS-12 and D-AAS-25. This was also observed in the ^{17}O NMR spectrum where the labeled water adsorbed at the defects sites (Fig. 2e). Subsequently, as the temperature continued to rise, a second weight loss step was observed, around 350 °C (Supplementary Fig. 12). This step signifies the onset of dehydroxylation, which involves the release of water following the breakdown of two surface hydroxyl groups (−OH) within the material's structure[47]. The weight loss attributed to dehydroxylation followed the same increasing trend as the loss due to adsorbed water, escalating from AAS (1.3%) to D-AAS-12 (3.4%) and further to D-AAS-25 (4.2%) (Supplementary Fig. 12). The introduction of defects increased the concentration of surface hydroxyl groups, also observed from the ^1H NMR studies. This ultimately contributed to a higher degree of dehydroxylation and the associated weight loss.

Quantifying defects via oxygen capture capacity

The relative quantification of oxygen vacancies in AAS and defective AASs was determined through the estimation of their oxygen capture capacity using O_2 temperature programmed desorption (TPD) studies (Supplementary Fig. 13). Initially, the catalyst's surface was saturated with O_2 gas, with the oxygen vacancies and defect sites within the material serving as the adsorption sites for the O_2 molecules. Subsequently, the temperature of the catalyst was gradually increased, causing the desorption of gases that were then detected; the amount of O_2 desorbed will be directly proportional to the concentration of oxygen vacancies present. The desorption signals obtained from the thermal conductivity detector (TCD) for all three samples exhibited two partially overlapping broad peaks around 100 °C, along with a broader peak around 300 °C, extending its tail up to 700 °C (Supplementary Fig. 13). The initial broad peak corresponds to the desorption of water molecules, which were introduced as impurities during the O_2 purging step. The subsequent desorption peak corresponds to the release of chemisorbed O_2 molecules from the surface, resulting from the presence of oxygen vacancies. The identification of water and oxygen molecules was also confirmed by a mass spectrometer coupled with the TPD instrument. In the case of D-AAS-12 and D-AAS-25, the desorption peak at higher temperatures exhibited a main peak within the range of 280–290 °C, accompanied by a shoulder peak at ~390 °C and another shoulder at around 506 °C (Supplementary Fig. 13). The desorption peak associated with O_2 was further deconvoluted into three distinct peaks for all three catalysts (Supplementary Fig. 13). The desorption peak within the range of 280–290 °C was attributed to the desorption of O_2 molecules adsorbed on the oxygen vacancies,

bonded to Si or Al atoms adjacent to the vacancies[86,87]. The shoulder peak at around 390 °C likely arises from the desorption of O_2 molecules adsorbed within oxygen vacancies exhibiting different chemical environments, possibly stabilized or buried deeper within the pores[88,89]. The origin of the shoulder peak at ~506 °C remains unclear, although it may be attributed to the desorption of peroxy radical species formed following the reaction of O_2 with surface radical species. All the observed desorption peaks were also present in the case of AAS, suggesting the existence of naturally formed defects during the synthesis process (Supplementary Fig. 13). Furthermore, the amount of O_2 desorbed during the TPD analysis was found to be highest in D-AAS-25, with a value of 2.1 ± 0.11 mmol g^{-1}, followed by D-AAS at 1.7 ± 0.1 mmol g^{-1}, and AAS at 0.15 ± 0.08 mmol g^{-1} (Supplementary Fig. 13).

Determination of acidic strength by ammonia TPD analysis

To gain insights into the influence of defects on the acidic strength of the materials, we conducted an ammonia TPD study[47] (Supplementary Fig. 14). Initially, the catalyst's surface was saturated with NH_3 gas, with the Brønsted acidic sites and surface hydroxyl groups within the material serving as the adsorption sites for the NH_3 molecules. Subsequently, the temperature of the catalyst was gradually increased, causing desorption of NH_3 which was then detected. Through analysis of Gaussian-deconvoluted traces, we were able to derive quantitative insights into the acidic strength of D-AAS and AAS. In the high-temperature strong acid region (above 310 °C)[47], all materials exhibited two distinct desorption peaks (Supplementary Fig. 14). In the case of D-AAS-12, the desorption peak was observed at a higher temperature compared to AAS. This shift in the desorption peak, observed in D-AAS-12 (343 and 493 °C) compared to AAS (at 292 and 427 °C), indicated a stronger bonding of NH_3 and, consequently, a higher acidic strength. However, as the defect concentration was further increased in D-AAS-25, the desorption peak temperature decreased (320 and 437 °C), suggesting a decrease in acidic strength. This trend was also reflected in the total amount of desorbed ammonia. The quantity of NH_3 adsorbed increased from AAS (0.6 ± 0.02 mmol g^{-1}) to D-AAS-12 (1.1 ± 0.06 mmol g^{-1}) and subsequently decreased in D-AAS-25 (0.8 ± 0.1 mmol g^{-1}) (Supplementary Fig. 14). These findings indicated that D-AAS-12 exhibits superior acidic behavior compared to both AAS and D-AAS-25. These results highlight the significance of an optimal defect concentration in enhancing the acidity of AAS. The observed phenomenon can be attributed to the loss of aluminum sites resulting from an increased defect concentration. Consequently, the introduction of defects in AAS has two opposing effects: it creates defects that improve the acidity of the Brønsted acidic sites, while simultaneously leading to a reduction in the number of aluminum sites (Supplementary Table 1).

Assessing the impact of defect creation in catalysis using four acid-catalyzed reactions

To elucidate the impact of defects on AAS acidity and, consequently, catalytic activity, a series of four acid-catalyzed reactions were conducted. The ring-opening reaction of styrene oxide (Fig. 3a), was chosen as our model system to identify the most effective catalyst with an optimal defect concentration. D-AAS-12 exhibited a superior performance compared to AAS, indicating an enhanced level of acidity. The conversion of styrene oxide reached 88% within 90 min, and subsequently plateaued at around 92% (Fig. 3a). On the other hand, AAS achieved a conversion of 54% in the same time frame, reaching a maximum value of 74% after 240 min (Fig. 3a). The substantial disparity in conversion and kinetics between D-AAS-12 and AAS underscores the influence of defects in augmenting the acidity and catalytic activity of AAS.

However, as the defect concentration was increased in D-AAS-25, a decline in catalytic activity and kinetics was observed, yielding a
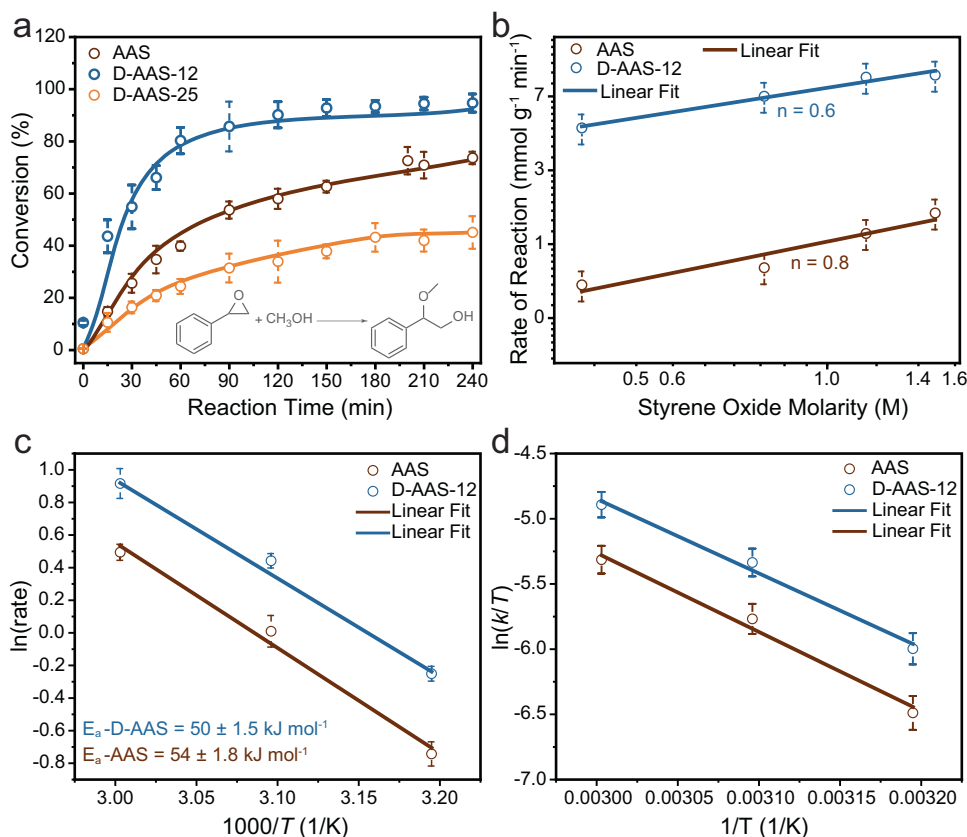
Fig. 3 | Catalytic performance and kinetic analysis of styrene oxide ring-opening by AAS and defective AAS. a Styrene oxide ring-opening catalyzed by AAS, D-AAS-12, and D-AAS-25, The solid lines are guidelines, not fit lines. **b** Order of the reaction, **c** Arrhenius plot for the activation energy, and **d** Eyring plot for entropy change for styrene oxide ring-opening reaction catalyzed by AAS and D-AAS-12. Error bars: Standard deviation calculated from data of at least three repeated experiments for all the figures.

conversion of 31% within 90 min in comparison to AAS (Fig. 3a). This reduction can be attributed to its higher Si/Al ratio due to loss of some Al sites from the framework. The increased Si/Al ratio adversely affects the acidity, as also evidenced by the NH_3 TPD. These results emphasize the significance of striking an optimal balance in defect concentration to achieve the desired catalytic performance. Subsequently, the reaction parameters, such as temperature and initial concentration of styrene oxide, were systematically varied to optimize the reaction conditions. The initial amount of styrene oxide was varied from 2.2 to 8.8 mmol while monitoring the resulting conversion and reaction kinetics. Maximum conversion and reaction kinetics were attained at an initial styrene oxide amount of 2.2 mmol, with a subsequent decrease in performance observed as the amount of styrene oxide was increased (Supplementary Fig. 15a). This phenomenon can be attributed to the fact that a smaller quantity of styrene oxide undergoes faster conversion, leading to the attainment of maximum conversion at an earlier stage.

However, upon calculating the turnover number (TON), it was discovered that the TON increased from 2.2 to 6.6 mmol of styrene oxide. Subsequently, as the amount of styrene oxide was further increased, the TON continued to rise; however, the rate of TON increase was not as pronounced as observed in the earlier range (Supplementary Fig. 15b). The styrene oxide quantity was standardized at 6.6 mmol, while the reaction temperature was varied within the range of 40–60 °C. A progressive elevation in temperature yielded notable enhancements in conversion, reaction kinetics, and TON for both AAS and D-AAS-12 (Supplementary Fig. 16). Intriguingly, D-AAS-12 consistently outperformed AAS across all temperature conditions, exhibiting a superior ability to convert a higher number of reactant

molecules i.e., TON, and at a faster reaction rate i.e., kinetics (Supplementary Fig. 16).

By examining the order of the reaction, we attempted to gain a deeper understanding of the interaction between reactant molecules and the catalyst surface, thereby elucidating the underlying mechanisms[90,91]. We performed calculations to ascertain the order of the reaction concerning styrene oxide for both AAS and D-AAS-12 while keeping methanol concentration constant (Fig. 3b). The order was obtained from the log plot of the rate of the reaction with the initial styrene oxide concentration. The calculation was performed using Eqs. (1)–(3):

$$\text{Rate}\,(k) \propto [\text{Styrene oxide}\,(M)]^n \tag{1}$$

$$\text{Rate}\,(k) = C \times [\text{Styrene oxide}\,(M)]^n \tag{2}$$

$$\ln(k) = \ln(C) + n \times \ln(M) \tag{3}$$

Here, k is the rate of reaction, C is a constant, M is the initial molarity of styrene oxide, and n is the order of the reaction.

The order of the reaction was found to decrease from AAS (0.8 ± 0.08) to D-AAS-12 (0.6 ± 0.04), which indicated better surface coverage or adsorption of styrene oxide on D-AAS-12, which helped in enhancing the catalytic activity as compared to AAS (Fig. 3b). We then calculated the activation energy of the reaction using the Arrhenius equation to quantitatively assess the energy barrier associated with the reaction for both AAS and D-AAS-12 (Fig. 3c). It showed similar activation energy values for both catalysts, suggesting that AAS and D-

AAS-12 follow similar reaction mechanisms and energy profiles (Fig. 3c). The close resemblance in the activation energies of AAS and D-AAS-12, while informative, does not provide a comprehensive explanation for the observed enhancement in catalytic activity. This suggests that the heightened acidity of D-AAS-12 likely exerts its influence on various reaction steps beyond solely impacting the rate-determining step.

To gain deeper insights into the intricate details of the reaction mechanism, we employed the Eyring plot analysis to examine the entropy change for both AAS and D-AAS-12[92]. This comprehensive analysis allowed us to discern the specific step in the reaction mechanism where the catalyst actively participated, shedding light on its crucial role. We derived the pre-exponential factor (A) from the Arrhenius plot (Fig. 3c) for D-AAS-12 and AAS. By utilizing Eqs. (4)–(7), we calculated the entropy change associated with the reaction.

$$k = \frac{k_B T}{h} e^{-\left(\frac{\Delta H^{\ddagger}}{RT}\right)} e^{\left(\frac{\Delta S^{\ddagger}}{R}\right)} \quad (4)$$

$$\ln\left(\frac{k}{T}\right) = \ln\left(\frac{k_B}{h}\right) - \frac{\Delta H^{\ddagger}}{RT} + \frac{\Delta S^{\ddagger}}{R} \quad (5)$$

$$\Delta H^{\ddagger} = slope \times R \quad (6)$$

$$\Delta S^{\ddagger} = R \ln A - R \ln\left(\frac{k_B T}{h}\right) - R \quad (7)$$

The Eyring plot analysis for the entropy change exhibited a moderately negative value for both D-AAS-12 ($-93.9 \pm 2.3\,\mathrm{J\,K^{-1}\,mol^{-1}}$) and AAS ($-88.2 \pm 1.9\,\mathrm{J\,K^{-1}\,mol^{-1}}$), indicating that they function as specific acids in the initial step of the reaction rather than in the rate-limiting step (Fig. 3d).

We also investigated the reproducibility of D-AAS-12 synthesis across different batches by conducting styrene oxide ring-opening reactions for three independent batches of D-AAS-12. We observed consistent conversion rates with all three batches of D-AAS-12, affirming the reliability and repeatability of the synthesis process (Supplementary Fig. 17). To evaluate the practical viability of the D-AAS-12 catalyst, we conducted an assessment of its recyclability. It revealed that D-AAS-12 exhibited sustained catalytic activity for at least 10 cycles (Supplementary Fig. 18), showcasing its inherent stability and immense potential for practical applications. We evaluated the impact of acid treatment on catalysis by conducting the styrene oxide ring-opening reaction with acid-treated AAS. The acid-treated AAS exhibited comparable activity to untreated AAS, indicating minimal changes from the acid treatment (Supplementary Fig. 19). In contrast, D-AAS-12 without acid wash displayed negligible activity, highlighting the importance of acid wash in removing Mg-byproducts that are formed during the defect creation (Supplementary Fig. 19). Control experiments using Mg powder as a catalyst also showed minimal activity (Supplementary Fig. 19), confirming the role of defects in enhancing acidity and activity in D-AAS-12.

Synergy between defects and textural properties in AAS during catalysis

While the epoxide ring opening reaction provided insight into the impact of defects on catalytic performance, it did not elucidate the significant influence of pore size and surface area on catalytic behavior. Hence, we sought to investigate the mass diffusion characteristics in conjunction with the acidic properties of D-AAS-12 relative to AAS. To comprehensively assess these attributes, we selected a diverse range of challenging acid-catalyzed reactions, employing reactant molecules possessing distinct sizes and functionalities. Our initial selection of the Friedel−Crafts alkylation reaction was predicated upon its

involvement in the condensation of two six-membered carbon rings. This reaction necessitated not only a good level of acidity but also the presence of a mesoporous structure capable of accommodating the resulting larger product molecule (Fig. 4a). In this reaction, D-AAS-12 demonstrated superior performance compared to AAS, highlighting its enhanced acidity and mesoporous structural attributes relative to AAS (Fig. 4a).

Subsequently, we conducted a comparative analysis of the catalytic activities of AAS and D-AAS-12 in the synthesis of jasminaldehyde. This reaction, in addition to the involvement of the six-membered carbon ring, introduced heptanal as another reactant. This allowed us to probe whether the alterations in textural properties and acidic strength associated with D-AAS-12 retained their cooperative effect when catalyzing the activation of a larger reactant molecule featuring an extended open carbon chain. In this case, D-AAS-12 consistently outperformed AAS in terms of reaction kinetics and overall conversion (Fig. 4b).

Finally, we turned our attention to a reaction involving the condensation of two six-membered carbon rings, accompanied by the formation of a double bond. The formation of this double bond imposed geometric constraints on the product molecule and required a specific coupling of two reactant molecules to overcome the steric hindrances posed by side chains. The D-AAS-12 and AAS were both subjected to testing in the context of acid-catalyzed vesidryl synthesis, with D-AAS-12 once again surpassing AAS (Fig. 4c). D-AAS-12 and AAS were then compared against conventional solid acids for vesidryl synthesis (Supplementary Table 3). The mesoporous morphology and strong acidity of AAS, in cooperation with defects, facilitated superior catalytic activity, even at lower reaction temperatures and lower catalyst amounts, in contrast to conventional solid acid catalysts. Collectively, these reactions underscored the superior attributes of D-AAS-12 when compared to AAS, highlighting the synergistic interplay between its structural characteristics and enhanced acidic strength. This superior performance across a range of reactions demonstrates how the cooperative enhancement of structural and acidic properties on the introduction of defects in AAS expands the applicability of solid acid catalysts in diverse acid-catalyzed reactions involving reactant molecules of varying sizes.

Probing molecular mechanisms: insights from in-situ FTIR analysis

To understand the intricate interplay between reactant molecules and defect sites, we undertook in-situ FTIR studies. These investigations aimed to elucidate the interaction dynamics between various molecular species and defect sites within the system. The obtained FTIR spectra of the samples, AAS and D-AAS-12, exhibited distinct peaks at 1131 and 1070 cm^{-1}, respectively. These peaks were attributed to the stretching mode of Al−O−Si and Si−O−Si bonds (Fig. 5a–c)[93–95]. Furthermore, an additional signal at 3742 cm^{-1} was observed, which originated from the stretching vibrations of Si−OH groups[96]. A broad signal spanning the range of 3000–3600 cm^{-1} indicated the presence of adsorbed water molecules on the surface of the catalyst[96]. Additionally, a weak signal at 964 cm^{-1} was detected, which could be ascribed to the stretching vibrations of Si−OH or Al−OH groups[97]. Of particular significance were the peaks at 1079 and 1198 cm^{-1}, corresponding to the transverse optical (TO) and longitudinal optical (LO) modes, respectively, of the asymmetric stretching of the Si−O−Si bond[98]. In the harmonic approximation, the TO and LO phonons are the points where the dielectric function of the medium peaks or drops, respectively. LO modes involve atoms vibrating parallel to the main axis of the lattice, while TO modes involve atoms vibrating perpendicular to this axis. Deconvolution of the peaks within the 900–1300 cm^{-1} region allowed us to analyze the relative areas associated with specific vibrational modes. Interestingly, the ratio of the area at 1131 cm^{-1} to that at 1070 cm^{-1} was found to be lower in the case
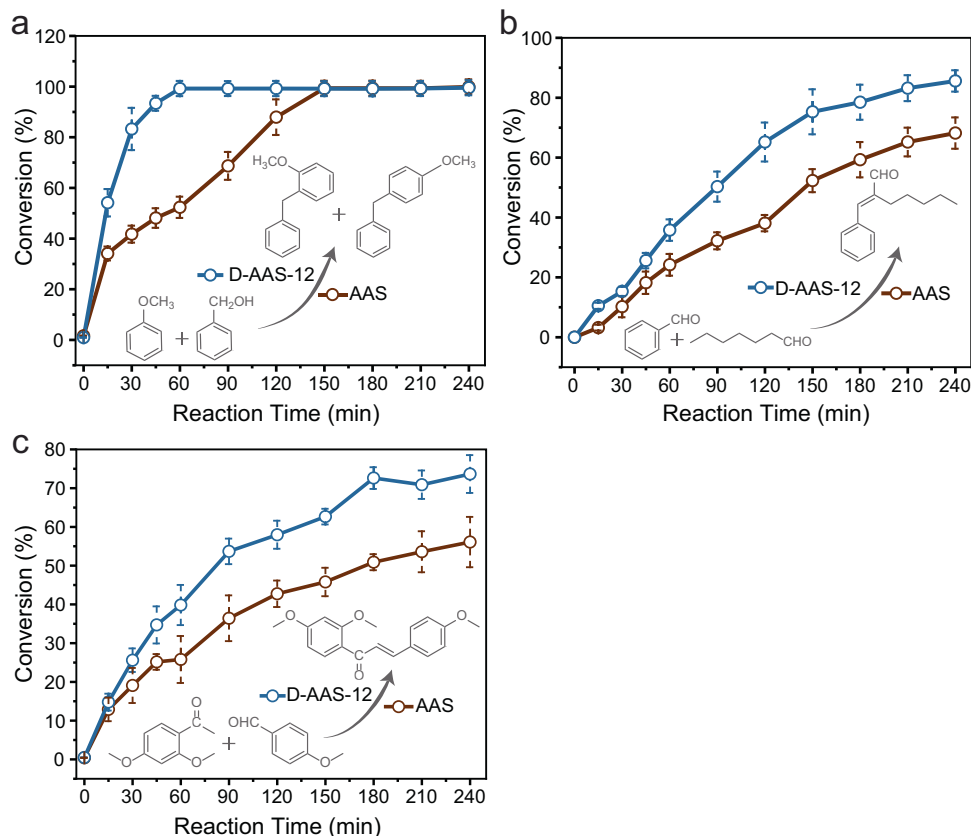
Fig. 4 | Catalytic activity of AAS and D-AAS-12 in various reactions. a Friedel−Crafts alkylation, **b** jasminaldehyde, and **c** vesidryl synthesis reactions catalyzed by AAS, and D-AAS-12. Error bars: Standard deviation calculated from data of at least three repeated experiments for all the figures.

of D-AAS-12 (0.39) compared to AAS (0.63). This observation suggested the occurrence of oxygen vacancies resulting from the rupture of Si−O−Al bonds (Fig. 5a−c). Upon the introduction of styrene oxide to the D-AAS-12 catalyst, a distinctive feature emerged in the form of a shoulder in the peak at 875 cm^{-1} (Fig. 5d, vertical dashed line in magnified Fig. 5e), which is known to correspond to epoxide ring vibrations[99]. This shoulder appeared at a lower wavenumber compared to the peak observed for pure styrene oxide. This spectral observation suggested an interaction between the epoxide ring and the oxygen vacancies present in the D-AAS-12 catalyst, consequently leading to the perturbation of the epoxide ring structure (Fig. 5d−f).

To gain further insights into the reaction progression, in-situ FTIR measurements were performed. These investigations enabled the real-time monitoring of the chemical transformations occurring within the system. After recording the baseline with the KBr pellet, we loaded the D-AAS-12 pellet, which had been diluted with KBr powder (details provided in the "Methods" section), into the in-situ FTIR reaction cell. Upon the addition of styrene oxide and methanol, we observed a noticeable change in the relative intensity of styrene oxide peaks compared to those observed with pure styrene oxide on D-AAS-12 (Fig. 5d, g). This variation occurred due to the differing baseline recording methods employed: while pure styrene oxide on D-AAS-12 utilized the D-AAS-12 pellet as the baseline, the in-situ FTIR experiments employed the KBr pellet. Consequently, the presence of signals from D-AAS-12 and methanol led to signal interference, resulting in the observed change in relative peak intensities of styrene oxide. Over time, a discernible reduction in the intensities of the peaks associated with the stretching vibrations of the epoxide ring at 1250 and 875 cm^{-1} was observed[99]. This decrease in peak intensity directly indicated the opening of the epoxide ring and its subsequent conversion into the product (Fig. 5g).

The in-situ FTIR studies provided insights into the intricate molecular-level interactions and the progression of reactions occurring on the D-AAS-12 catalyst. These findings have shed light on the pivotal role played by defect sites in facilitating desired chemical transformations. Based on the results of in-situ FTIR, we have proposed a reaction mechanism for the catalytic process of epoxide ring opening by D-AAS-12 (Fig. 5h). The initial step involves the adsorption of styrene oxide onto the surface of D-AAS-12. Subsequently, the acidic proton of D-AAS-12 protonates the oxygen atom within the epoxide moiety. This protonation event sets the stage for the subsequent step, wherein methanol acts as a nucleophile and launches an attack on the carbon atom of the epoxide ring, ultimately leading to its opening. The proton is subsequently transferred back to D-AAS-12, resulting in the desorption of the product from the catalyst surface. As a final step, the catalyst is regenerated, ready to initiate the next reaction cycle (Fig. 5h). This proposed mechanism emphasizes the critical role of D-AAS-12 as an acid catalyst, effectively facilitating the sequential processes of adsorption, protonation, and subsequent ring-opening of the epoxide functionality, ultimately leading to the formation of the product.

In this study, we successfully enhanced the acidic strength and catalytic activity of AAS by strategically tuning the oxygen vacancies through the magnesiothermic treatment method, introducing defects into the AAS material. Our approach proved highly effective in improving catalytic performance across a spectrum of acid-catalyzed reactions, including styrene oxide ring opening, vesidryl synthesis, Friedel-Crafts alkylation, and jasminaldehyde synthesis. Comprehensive characterization techniques allowed us to assess the properties of D-AAS. While the introduction of defects did not significantly alter the morphology or textural properties of AAS, it brought about distinct changes in optical and chemical properties, such as O$_2$ capture capability and acidic strength, which correlated with defect concentration.
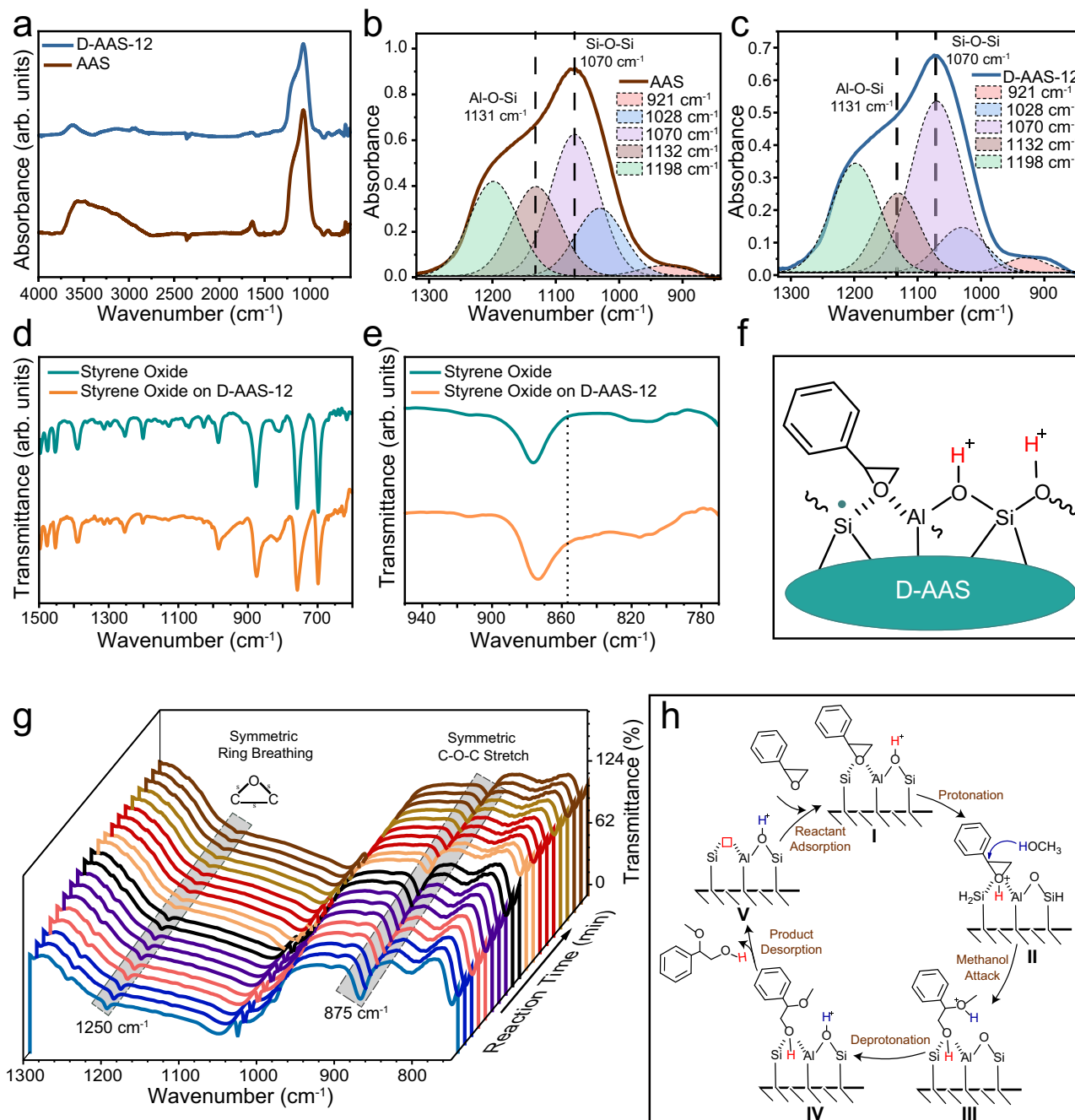
Fig. 5 | FTIR analysis and proposed mechanism of styrene oxide ring-opening. a FTIR spectra of AAS and D-AAS, Deconvulated FTIR spectra of **b** AAS, **c** D-AAS-12, the dashed lines indicate the peak corresponding to stretching vibrations of Al−O−Si (1131 cm⁻¹) and Si−O−Si (1070 cm⁻¹). **d, e** FTIR spectra of styrene oxide pure and adsorbed on D-AAS-12, the vertical dashed line shows the appearance of a shoulder in the 875 cm⁻¹ peak. **f** Proposed interactions of styrene oxide with the

defects centers of D-AAS-12. **g** Time-dependent in-situ FTIR of styrene oxide ring-opening reaction catalyzed by D-AAS-12, the shaded region in the spectra highlights the stretching vibrations of the epoxide ring at 1250 and 875 cm⁻¹, and the changes in these features over time. **h** Proposed reaction mechanism of styrene oxide ring-opening reaction catalyzed by D-AAS-12.

The catalyst exhibited a specific acidity order: D-AAS-12 > D-AAS-25 > AAS, underscoring the importance of optimizing defect concentration to achieve the desired acidity level in AAS. Solid-state NMR, XPS, EPR, and FTIR analyses offered valuable insights into defect nature, concentration, and their correlation with the aluminosilicate framework. Solid-state NMR spectroscopy revealed changes in the Al composition introduced by defect formation, with an increase in Al(IV) sites in D-AAS-12, which likely corresponds to its increased acidity. The increased acidity and the presence of oxygen vacancies in D-AAS-12 also enabled facile, uniform ^{17}O labeling of Si−OH, Si−O−Al, and

Si−O−Si species using $H_2{}^{17}O$ at room temperature, permitting the rapid acquisition of 1D ^{17}O and MQMAS solid-state NMR spectra.

The impact of defect creation on catalytic behavior was consistently demonstrated across four different reactions, with D-AAS consistently outperforming AAS. This highlights the superior synergistic effects between introduced defects and existing acidic sites within the D-AAS catalyst. In-situ FTIR analysis offered critical insights into molecular-level reaction mechanisms, particularly in the styrene oxide ring-opening reaction, where the shift in the epoxide ring's peak indicated an interaction between D-AAS-12 and styrene oxide.

In conclusion, our study underscores the potential of defect manipulation as a promising avenue for fine-tuning the acidity of amorphous aluminosilicates. The multifaceted characterization and catalytic studies presented here provide a comprehensive understanding of the role of defects in enhancing acidity and catalytic performance, offering valuable insights for the design of advanced catalysts tailored to specific reactions in heterogeneous catalysis.

Methods

Materials

Cetyltrimethylammonium bromide (CTAB, ≥99%; Sigma-Aldrich), Urea (≥99%; Sigma-Aldrich), Tetraethyl orthosilicate (TEOS, 98%; Sigma-Aldrich), Tris(2,4-pentanedionato)aluminum(III) (Al(acac)$_3$, >99.0%; Tokyo Chemical Industry (TCI)), p-Xylene (p-xylene for synthesis, 99%; Loba Chemie), Deionized water (H$_2$O; Milli-Q System; Millipore), Ethanol (99.9%, Changshu Hongsheng Fine Chemical Co. Ltd.), Magnesium powder (≥99%; Sigma-Aldrich), Methanol (anhydrous, 99.8%; Sigma-Aldrich), Styrene Oxide (>98.0%, Tokyo Chemical Industry (TCI)), 2′,4′-Dimethoxyacetophenone (97%; Sigma-Aldrich), p-Anisaldehyde (98.0%, Sigma-Aldrich), Anisole (>99.0%; Tokyo Chemical Industry (TCI)), Benzyl alcohol (ReagentPlus, ≥99%; Sigma-Aldrich), Benzaldehyde (ReagentPlus, ≥99%; Sigma-Aldrich), and Heptanal (>95.0%, Tokyo Chemical Industry (TCI)).

Synthesis of amorphous acidic aluminosilicates (AAS)

In a typical synthesis, a cationic detergent cetyltrimethylammonium bromide (CTAB) (500 mg) and urea (600 mg) were taken in a 500 mL round bottom (RB) flask[47]. Deionized water (5 mL) was then added to the RB and the solution was then stirred for 30 min using magnetic stirring (1400 r.p.m.). To this, a freshly prepared solution of TEOS (2.8 mmol) and Al(acac)$_3$ (2.8 mmol) in p-xylene (45 mL) was added dropwise under stirring (1000 r.p.m). The reaction mixture was then stirred (1000 r.p.m) at room temperature (RT) for 30 min. It was then refluxed at 120 °C for 12 h and subsequently cooled to RT. The white solid product was then isolated by centrifugation (15,356×g for 10 min). The product was then washed with ethanol (3 times), and DI water (3 times). This is followed by another final wash with ethanol. The solid product was then dried at 80 °C for 12 h in an oven. The dried solid product was then calcined at 750 °C (ramp: 5 °C min^{-1}) for 6 h in the air to remove the CTAB template (Supplementary Fig. 1)[47].

Synthesis of defective amorphous acidic aluminosilicates (D-AAS)

In a typical synthesis of D-AAS, AAS (200 mg) was mixed with magnesium (Mg) powder (24 and 50 mg for D-AAS-12 and D-AAS-25, respectively, where 12 and 25 represent the weight percentage of magnesium powder with respect to the weight of AAS)[43]. The AAS and Mg powders were thoroughly ground using a mortar pestle for 15 min. The ground powder was then transferred to an alumina boat. The boat was heated in a tube furnace at 650 °C for 5 h in a quartz tube in Argon flow (100 mL min^{-1}). The tube was then cooled to room temperature, and defective AAS, magnesium oxide (MgO), and magnesium orthosilicate (Mg$_2$SiO$_4$) powders were formed. MgO or Mg$_2$SiO$_4$ was then removed by dissolving it by stirring (700 r.p.m) the powder in a solution of hydrochloric acid (13 M, 14.5 mL) (to form MgCl$_2$), ethanol (224 mL), and DI water (20 mL) for 6 h. The solid product was then washed with ethanol (3 times), and DI water (3 times). This is followed by another final wash with ethanol. The solid product was then dried at 80 °C for 12 h in an oven. The dried powder was then stored under normal atmospheric conditions (Supplementary Fig. 2).

Characterization of AAS and D-AAS

All SEM imaging was performed using a Zeiss Ultra microscope at 3 kV with a working distance of 8 mm. Scanning transmission electron microscopy (STEM) analysis was carried out using FEI Tecnai operated

at an accelerating voltage of 200 kV. Elemental mapping was carried out using energy-dispersive X-ray spectroscopy (EDS). Samples were prepared by dispersing a small amount of solid powder in ethanol by sonicating for 10 s. The dispersion was drop-casted onto a holey carbon-coated 200 mesh copper TEM grid. PXRD patterns were obtained using a PANalytical X'Pert Pro powder X-ray diffractometer with Cu-Kα radiation. N$_2$ sorption measurements were performed using a Micromeritics 3-Flex surface analyzer (samples were degassed at 200 °C for 24 h under a vacuum before analysis). UV–Vis–DRS measurements were carried out using a JASCO UV–Vis/NIR spectrophotometer. XPS analysis was carried out using a Thermo Kα+ spectrometer with micro-focused and monochromated Al-Kα radiation (1486.6 eV) as the X-ray source. The sample was prepared by sprinkling solid powder on carbon tape. The carbon signal at 284.6 eV was used as an internal reference. Thermal gravimetric analysis (TGA) analysis was performed using a Mettler Toledo TGA instrument. In a typical analysis, 6–8 mg of sample was taken in an alumina crucible and was degassed at 120 °C for 1 h under Ar flow (50 mL min^{-1}). The temperature was then increased to 700 °C at the rate of 10 °C min^{-1} under Ar flow (50 mL min^{-1}). For the photoluminescence (PL) measurements, excitation was carried out at 400 nm (slit width 1 nm) using a Xenon lamp in FluoroLog®-3 (Horiba Jobin Yvon Inc.). The sample was prepared by dispersing the catalyst in ethanol (1 mg mL^{-1}) by sonicating it for 5 min. The dispersion (750 μL) was taken in a quartz cuvette followed by light excitation. The EPR spectra of all samples were recorded at room temperature using Bruker EMX micro X-band cw EPR spectrometer. The following conditions were used to record the EPR spectra of the catalyst, amount = 40 mg, power = 10.0 mW, number of scans = 5, microwave frequency = 9.331594 GHz, and Q-factor = 14,300. The solid sample powder was degassed in an EPR tube at 120 °C for 10 h before recording the EPR spectra. The magnesium content was also quantified using Agilent 7900 inductively coupled plasma mass spectrometry (ICP-MS). ICP-MS was done by digesting 1 mg of sample powder in 100 μL of concentrated HNO$_3$ at 80 °C for 6 h. The solution was then filtered to remove any suspended solid product and the filtered solution was diluted with DI water to make the final concentration 10 ppb. The instrument was calibrated by recording data using standard solutions of 0, 5, 10, 20, 50, and 100 ppb of metal salts.

Oxygen capture capacity (OCC) measurement

The oxygen capture capacity (OCC) measurements were done using Catalyst Analyzer BELCAT II coupled with a quadrupole mass spectrometer (Belmass). Catalyst (20 mg) was taken in a quartz tube and heated from 25 to 200 °C at a ramp rate of 10 °C min^{-1} under helium flow (30 mL min^{-1}). The catalyst was then kept at 200 °C for 1 h under helium flow (30 mL min^{-1}) to remove adsorbed surface impurities. The temperature was then reduced to −80 °C under helium flow (30 mL min^{-1}) followed by 10 min purging at −80 °C under helium flow (30 mL min^{-1}) to attain temperature stability. The catalyst was then exposed to oxygen gas (30 mL min^{-1}) at −80 °C for 30 min. The quartz tube was then purged by flowing helium gas (30 mL min^{-1}) to remove the physisorbed oxygen molecules. The catalyst was then heated from −80 to 700 °C at a ramp rate of 10 °C min^{-1} under helium flow (30 mL min^{-1}), and the desorbed gases were detected by thermal conductivity detector (TCD) and quadrupole mass spectrometer (belmass). The desorbed gases were quantified by TCD signal, which was calibrated by doing a five-point calibration by introducing known concentrations of gases.

Acidic strength measurement by ammonia temperature programmed desorption (NH$_3$-TPD)

The acidic strength measurements by ammonia temperature programmed desorption (NH$_3$-TPD) were done using Catalyst Analyzer BELCAT II coupled with a Quadrupole mass spectrometer (Belmass). Catalyst (28 mg) was taken in a quartz tube and heated from 25 to

200 °C at a ramp rate of 10 °C min⁻¹ under helium flow (30 mL min⁻¹). The catalyst was then kept at 200 °C for 1 h under helium flow (30 mL min⁻¹) to remove adsorbed surface impurities. The temperature was then reduced to 50 °C under helium flow (30 mL min⁻¹) followed by 10 min purging at 50 °C under helium flow (30 mL min⁻¹) to attain temperature stability. The catalyst was then exposed to 5% NH_3 (in He) gas (30 mL min⁻¹) at 50 °C for 30 min. The quartz tube was then purged by flowing helium gas (30 mL min⁻¹) to remove the physisorbed NH_3 molecules. The catalyst was then heated from 50 to 700 °C at a ramp rate of 10 °C min⁻¹ under helium flow (30 mL min⁻¹), and the desorbed gases were detected by thermal conductivity detector (TCD) and quadrupole mass spectrometer (belmass). The desorbed gases were quantified by TCD signal, which was calibrated by doing a five-point calibration by introducing known concentrations of gases.

Solid-state NMR spectroscopy

AAS, D-AAS-12, D-AAS-25, and D-AAS-12-¹⁷O samples were prepared for solid-state NMR by degassing at 200 °C for 12 h under vacuum. Helium gas was then flowed at 200 °C for 60 min followed by cooling to room temperature under helium. D-AAS-12-¹⁷O was prepared by treating D-AAS-12 with 90% ¹⁷O-labeled water ($H_2^{17}O$). After the above-mentioned treatment at 200 °C and cooling, 50 µL of $H_2^{17}O$ was added under stirring. The sample was then stirred at room temperature for 60 min followed by the removal of excess water by flowing He gas at 120 °C for 60 min under stirring. The samples were then packed into rotors in a glove box under an Ar atmosphere.

All solid-state NMR experiments were performed at 18.8 T with $\nu_{0,1H}$ = 799.71 MHz, $\nu_{0,27Al}$ = 200.39 MHz, and $\nu_{0,17O}$ = 108.41 MHz. ¹H chemical shifts were referenced with respect to neat tetramethylsilane with Adamantane as a secondary chemical shift standard at 1.92 ppm. ²⁷Al and ¹⁷O chemical shifts were indirectly referenced using the IUPAC recommended standard frequency ratios[100]. Spectra were processed in Bruker TopSpin 3.6.3. One- and two-dimensional (1D and 2D) ¹H NMR, and 2D ¹H–²⁷Al solid-state NMR experiments were performed at 50 kHz magic angle spinning (MAS) frequency using a 1.3 mm HXY probe in ¹H–²⁷Al configuration. 1D ¹H spectra were obtained using a rotor-synchronized spin echo pulse sequence. ¹H π/2 and π pulse lengths of 2.5 and 5 µs, respectively, were used. 2D ¹H-¹H spin diffusion spectra using a standard three-pulse sequence with the indicated spin diffusion periods. 2D spin diffusion spectra were acquired with 8 scans per increment, 256 hypercomplex t_1 increments (using STATES-TPPI), and a t_1-increment size of 40 µs (25 kHz indirect spectral width). ¹H–¹H single quantum– double quantum correlation spectrum of D-AAS-12 was obtained using one rotor cycle of back-to-back (BABA) recoupling[101]. ¹H detected 2D ¹H–²⁷Al correlation spectra were acquired using the dipolar refocused insensitive nuclei enhanced by polarization transfer (D-RINEPT) pulse sequence[65,66,102]. ²⁷Al central transition selective π/2 and π pulse lengths of 4.5 and 9 µs, respectively, were used. 800 µs of $SR4_1^2$ dipolar recoupling[103] was applied at the second-order rotary resonance recoupling condition (100 kHz rf). Rotor-assisted population transfer (RAPT)[104] was used to enhance the ²⁷Al central transition polarization prior to the INEPT transfer, using WURST pulses (2 rotor period duration, ±250 kHz offset, ca.19 kHz rf field). A recycle delay of 0.3 s was used. 64 t_1-increments (20 µs steps) were acquired with 128 (AAS) or 256 (D-AAS-12) scans per increment.

1D ²⁷Al and all ¹⁷O solid-state NMR experiments were performed at 16 kHz MAS frequencing using a 3.2 mm HXY probe. Samples were packed into 3.2 mm thin-wall Phoenix NMR rotors. 1D ²⁷Al solid-state NMR experiments were performed with a short 10° tip angle pulse (1.4 µs pulse length) to ensure quantitative excitation. A recycle delay of 2 s was found to be quantitative under these conditions. 1D ²⁷Al spectra of AAS, D-AAS-12, and D-AAS-12-¹⁷O were acquired with 512 scans, whereas the corresponding spectrum of D-AAS-25 was obtained with 1024 scans due to a relatively lower signal-to-noise ratio with this sample. A 1D ²⁷Al NMR spectrum of the broad, low-intensity

probe background signal was subtracted from all the 1D ²⁷Al spectra before further analysis. 1D ²⁷Al NMR spectra were fit to normal Czjzek distributions[105] (simple model) using ssNake v1.4[106]. Further details are provided in the figure caption. The 1D ¹⁷O solid-state NMR was obtained using a RAPT spin echo pulse sequence using a central transition selective π/2 pulse length of 6.5 µs; RAPT was applied using a 2-rotor period WURST pulse with a ± 250 kHz offset and ca. 22 kHz rf field. 2D ¹⁷O triple quantum magic angle spinning (3QMAS) spectrum was acquired using a shifted-echo MQMAS pulse sequence[72,73]. 3Q excitation and 3Q-SQ conversion pulses with pulse durations of 3.5 and 1.4 µs were applied at ca. 70 kHz rf. 32 t_1-increments were acquired with an increment duration of one rotor period (62.5 µs) and 1440 scans per increment and 0.5 s recycle delay, corresponding to a total acquisition time of ca. 6.5 h.

AAS or D-AAS catalyzed styrene oxide ring opening by methanol

AAS or D-AAS (15 mg) was taken in a Schlenk flask, degassed at 120 °C for 1 h to remove adsorbed moisture from the surface, and subsequently cooled under N_2 to 30 °C. Absolute methanol (5 mL) was added, and the flask was sonicated for 30 seconds. The flask was then heated to 60 °C. Styrene oxide (500 µL) was added to this flask under stirring and the reaction progress was monitored by withdrawing samples at different time points (0, 15, 30, 45, 60, 90, 120, 150, 180, and 240 min). All the products were identified by an Agilent 7890B GC–MS.

Recyclability test. Following each cycle, the solid catalyst underwent isolation via centrifugation at 15,356×g for 5 min, coupled with a thorough washing with methanol (5 mL) repeated twice to remove any adsorbed reactant or product molecules from the surface of the catalyst. Subsequently, the washed catalyst was redispersed in anhydrous methanol (5 mL) through 30 s of sonication, initiating a fresh cycle of the styrene oxide ring-opening reaction.

AAS or D-AAS catalyzed synthesis of 2′,4,4′-trimethoxychalcone (Vesidryl)

AAS or D-AAS-12 (20 mg) was taken in a Schlenk flask, degassed at 120 °C for 1 h to remove adsorbed moisture from the surface, and subsequently maintained under N_2 at 120 °C. 2,4-dimethoxy acetophenone (DMA) (3.4 mmol) was dissolved in p-Anisaldehyde (3.7 mmol) and then added to the reaction flask. the reaction progress was monitored by withdrawing samples at different time points (0, 15, 30, 45, 60, 90, 120, 150, 180, and 240 min). All the products were identified by an Agilent 7890B GC–MS.

AAS or D-AAS catalyzed Friedel−Crafts alkylation of anisole by benzyl alcohol

AAS or D-AAS-12 (10 mg) was taken in a Schlenk flask, degassed at 120 °C for 1 h to remove adsorbed moisture from the surface, and subsequently maintained under N_2 at 30 °C. Anisole (25 mmol) and benzyl alcohol (1.68 mmol) were mixed and then added to the Schlenk flask. The flask was then sonicated for 30 s. The flask was then dipped into an oil bath preheated at 120 °C, and the reaction progress was monitored by withdrawing samples at different time points (0, 15, 30, 45, 60, 90, 120, 150, 180, and 240 min). All the products were identified by an Agilent 7890B GC–MS.

AAS or D-AAS catalyzed synthesis of jasminaldehyde

AAS or D-AAS (50 mg) was taken in a Schlenk flask and degassed at 120 °C for 1 h to remove adsorbed moisture from the surface. The flask was then heated under N_2 to 125 °C. Benzaldehyde (15 mmol) and heptanal (3 mmol) were pre-mixed and then added to the reaction flask. The reaction progress was monitored by withdrawing samples at different time points (0, 15, 30, 45, 60, 90, 120, 150, 180, and 240 min). All the products were identified by an Agilent 7890B GC–MS.

In-situ Fourier transform infrared (FTIR) experimental

In-situ Fourier transform infrared (FTIR) measurements were carried out to study the nature of defect sites in D-AAS, the interaction of reactant molecules (styrene oxide) with the defect sites in D-AAS, and the reaction progress (styrene oxide ring opening) over D-AAS. In-situ FTIR measurements were performed using a Specac high-temperature transmission IR reaction cell with ZnSe windows and JASCO FT/IR-4700 equipment. KBr powder was pressed into a pellet of 13 mm diameter, and the pellet was then inserted into Specac's high-temperature transmission IR reaction cell. The baseline was then recorded with 400 scans and 2.0 cm^{-1} resolution. For catalyst analysis, a pellet was prepared by diluting D-AAS or AAS (1 mg) with KBr (200 mg) powder, by grinding them using a mortar pestle. The pellet was then inserted into the Specac's high-temperature transmission IR reaction cell followed by heating the pellet at 120 °C for 1 h under Ar flow (mL min^{-1}). The temperature of the pellet was then reduced to 30 °C under Ar flow (mL min^{-1}) and the IR spectrum was then recorded with 400 scans and 2.0 cm^{-1} resolution. To study the interaction of styrene oxide with the catalyst, the same heating and baseline procedure was used, and once the temperature of the pellet was reduced to 30 °C, 10 μL of styrene oxide was added to the catalyst pellet. The pellet was then inserted into the IR cell followed by purging of the IR cell by Ar flow (50 mL min^{-1}) for 10 min. The gas flow was then stopped and the inlet and outlet valves of the IR cell were closed. The IR spectrum was then recorded with 400 scans and a 2.0 cm^{-1} resolution. The styrene oxide ring-opening reaction by methanol catalyzed by D-AAS was studied by following the same heating and baseline procedure, and once the temperature of the pellet was reduced to 30 °C, 10 μL of styrene oxide and 100 μL of methanol was added to the catalyst pellet. The pellet was then inserted into the IR cell followed by purging of the IR cell by Ar flow (50 mL min^{-1}) for 10 min. The gas flow was then stopped and the inlet and outlet valves of the IR cell were closed. The temperature of the IR cell was then increased to 60 °C and the IR spectrum was then recorded with 400 scans and a 2.0 cm^{-1} resolution.

Data availability

The data that support the findings of this work are available within the article, its supplementary information file (Supplementary Figs. 1–19, Supplementary Tables 1 –3), as well as the source data file. The data are also available from the corresponding authors upon request. Source data are provided with this paper.

References

1. Chizallet, C., Bouchy, C., Larmier, K. & Pirngruber, G. Molecular views on mechanisms of brønsted acid-catalyzed reactions in zeolites. *Chem. Rev.* **123**, 6107–6196 (2023).
2. Li, Y. & Yu, J. New stories of zeolite structures: their descriptions, determinations, predictions, and evaluations. *Chem. Rev.* **114**, 7268–7316 (2014).
3. Pérez-Ramírez, J., Christensen, C. H., Egeblad, K., Christensen, C. H. & Groen, J. C. Hierarchical zeolites: enhanced utilisation of microporous crystals in catalysis by advances in materials design. *Chem. Soc. Rev.* **37**, 2530–254 (2008).
4. Gallego, E. M. et al. "Ab Initio" synthesis of zeolites for, pre-established catalytic reactions. *Science* **355**, 1051–1054 (2017).
5. Chizallet, C. & Raybaud, P. Pseudo-bridging silanols as versatile Brønsted acid sites of amorphous aluminosilicate surfaces. *Angew. Chem. Int. Ed.* **48**, 2891–2893 (2009).
6. Huang, J., van Vegten, N., Jiang, Y., Hunger, M. & Baiker, A. Increasing the Brønsted acidity of flame-derived silica/alumina up to zeolitic strength. *Angew. Chem. Int. Ed.* **49**, 7776–7781 (2010).
7. Wang, Z. et al. acid sites based on penta-coordinated aluminum species. *Nat. Commun.* **7**, 13820 (2016).
8. Valla, M. et al. Atomic description of the interface between silica and alumina in aluminosilicates through dynamic nuclear polarization surface-enhanced NMR spectroscopy and first-principles calculations. *J. Am. Chem. Soc.* **137**, 10710–10719 (2015).
9. Li, S. et al. Brønsted/Lewis acid synergy in dealuminated HY zeolite: a combined solid-state NMR and theoretical calculation study. *J. Am. Chem. Soc.* **129**, 11161–11171 (2007).
10. Dionigi, F. et al. In-situ structure and catalytic mechanism of NiFe and CoFe layered double hydroxides during oxygen evolution. *Nat. Commun.* **11**, 2522 (2020).
11. Wang, Z. et al. Revealing Brønsted acidic bridging SiOHAl groups on amorphous silica–alumina by ultrahigh field solid-state NMR. *J. Phys. Chem. Lett.* **12**, 11563–11572 (2021).
12. Yakimov, A. V. et al. Structure and framework association of Lewis acid sites in MOR zeolite. *J. Am. Chem. Soc.* **144**, 10377–10385 (2022).
13. Li, X. et al. Acid catalysis over low-silica faujasite zeolites. *J. Am. Chem. Soc.* **144**, 9324–9329 (2022).
14. Castro, M. J. M-. et al. Hierarchical catalysts prepared by inter-zeolite transformation. *J. Am. Chem. Soc.* **144**, 5163–5171 (2022).
15. Jain, R., Mallette, A. J. & Rimer, J. D. Controlling nucleation pathways in zeolite crystallization: seeding conceptual methodologies for advanced materials design. *J. Am. Chem. Soc.* **143**, 21446–21460 (2021).
16. Chen, C. -T. et al. Reaction kinetics regulated formation of short-range order in an amorphous matrix during zeolite crystallization. *J. Am. Chem. Soc.* **143**, 10986–10997 (2021).
17. Chen, K., Gan, Z., Horstmeier, S. & White, J. L. Distribution of aluminum species in zeolite catalysts: ^{27}Al NMR of framework, partially-coordinated framework, and non-framework moieties. *J. Am. Chem. Soc.* **143**, 6669–6680 (2021).
18. Hong, X. et al. Direct synthesis of aluminosilicate IWR zeolite from a strong interaction between zeolite framework and organic template. *J. Am. Chem. Soc.* **141**, 18318–18324 (2019).
19. Kemp, K. C., Mayoral, A. & Hong, S. B. Unveiling the structural characteristics of intergrowth zeolites synthesized in the presence of isopropylimidazolium-based cations and fluoride anions. *J. Am. Chem. Soc.* **145**, 23300–23307 (2023).
20. Castro, M. J. M.-, Qie, Z., Fan, X., Linares, N. & Martínez, J. G.- Tunable hybrid zeolites prepared by partial interconversion. *Nat. Commun.* **14**, 1256 (2023).
21. Chitac, R. G. et al. Synthetic control of the defect structure and hierarchical extra-large-/small-pore microporosity in aluminosilicate zeolite SWY. *J. Am. Chem. Soc.* **145**, 22097–22114 (2023).
22. Ma, Y. et al. Design of an organic template for synthesizing ITR zeolites under Ge-free conditions. *J. Am. Chem. Soc.* **145**, 17284–17291 (2023).
23. Jain, R. et al. In situ imaging of faujasite surface growth reveals unique pathways of zeolite crystallization. *J. Am. Chem. Soc.* **145**, 1155–1164 (2023).
24. Yeh, B. et al. Structure and site evolution of framework Ni species in MIL-127 MOFs for propylene oligomerization catalysis. *J. Am. Chem. Soc.* **145**, 3408–3418 (2023).
25. Zornes, A. et al. Impact of low-temperature water exposure and removal on zeolite HY. *J. Am. Chem. Soc.* **146**, 1132–1143 (2024).
26. Zheng, Y., Moya, A. V.-, Garrido, J. C. H.-, Mon, M. & Leyva-Pérez, A. Silver-exchanged zeolite Y catalyzes a selective insertion of carbenes into C–H and O–H bonds. *J. Am. Chem. Soc.* **145**, 24736–24745 (2023).
27. Leung, K. C. et al. Confined Ru sites in a 13X zeolite for ultrahigh H$_2$ production from NH$_3$ decomposition. *J. Am. Chem. Soc.* **145**, 14548–14561 (2023).
28. Ma, C. et al. Fluoride- and seed-free synthesis of pure-silica zeolite adsorbent and matrix using OSDA-mismatch approach. *J. Am. Chem. Soc.* **145**, 24191–24201 (2023).

29. Xie, C. et al. Defect chemistry in heterogeneous catalysis: recognition, understanding, and utilization. *ACS Catal.* **10**, 11082–11098 (2020).

30. Luo, Y. et al. Defect engineering to tailor metal vacancies in 2D conductive metal-organic frameworks: an example in electrochemical sensing. *ACS Nano* **16**, 20820–20830 (2022).

31. Yan, H. et al. Enhancing polyol/sugar cascade oxidation to formic acid with defect rich MnO_2 catalysts. *Nat. Commun.* **14**, 4509 (2023).

32. Böller, B., Durner, K. M. & Wintterlin, J. The active sites of a working Fischer–Tropsch catalyst revealed by operando scanning tunnelling microscopy. *Nat. Catal.* **2**, 1027–1034 (2019).

33. Chen, L. & Xu, Q. Fewer defects, better catalysis? *Science* **367**, 737 (2020).

34. Yang, J. et al. Single atomic vacancy catalysis. *ACS Nano* **13**, 9958–9964 (2019).

35. Zhu, Y. et al. Room-Temperature Photoluminescence Mediated by Sulfur Vacancies in 2D Molybdenum Disulfide. *ACS Nano* **17**, 13545–13553 (2023).

36. Wang, S. et al. H_2-reduced phosphomolybdate promotes room-temperature aerobic oxidation of methane to methanol. *Nat. Catal.* **6**, 895–905 (2023).

37. An, Z. et al. Highly active, ultra-low loading single-atom iron catalysts for catalytic transfer hydrogenation. *Nat. Commun.* **14**, 6666 (2023).

38. Chen, J. et al. Electron beam irradiation-induced formation of defect-rich zeolites under ambient condition within minutes. *Angew. Chem. Int. Ed.* **60**, 14858–14863 (2021).

39. Jia, J. et al. Heterogeneous catalytic hydrogenation of CO_2 by metal oxides: defect engineering—perfecting imperfection. *Chem. Soc. Rev.* **46**, 4631–4644 (2017).

40. Campbell, C. T. & Peden, C. H. F. Oxygen vacancies and catalysis on ceria surfaces. *Science* **309**, 713–714 (2005).

41. Tilley, R. J. D. Defects in solids. In *Encyclopedia of Inorganic Chemistry*, (ed. Scott, R. A.) 1–513 (John Wiley & Sons, Ltd., 2008).

42. Costa, I. C. M.- et al. Silanol defect engineering and healing in zeolites: opportunities to fine-tune their properties and performances. *Chem. Soc. Rev.* **50**, 11156–11179 (2021).

43. Mishra, A. K., Belgamwar, R., Jana, R., Datta, A. & Polshettiwar, V. Defects in nanosilica catalytically convert CO_2 to methane without any metal and ligand. *Proc. Natl Acad. Sci. USA* **117**, 6383–6390 (2020).

44. Belgamwar, R. et al. Defects tune the strong metal-support interactions in copper supported on defected titanium dioxide catalysts for CO_2 reduction. *J. Am. Chem. Soc.* **145**, 8634–8646 (2023).

45. Rawool, S. A., Yadav, K. K. & Polshettiwar, V. Defective TiO_2 for photocatalytic CO_2 conversion to fuels and chemicals. *Chem. Sci.* **12**, 4267–4299 (2021).

46. Polshettiwar, V. Dendritic fibrous nanosilica: discovery, synthesis, formation mechanism, catalysis, and CO_2 capture-conversion. *Acc. Chem. Res.* **55**, 1395–1410 (2022).

47. Maity, A., Chaudhari, S., Titman, J. J. & Polshettiwar, V. Catalytic nanosponges of acidic aluminosilicates for plastic degradation and CO_2 to fuel conversion. *Nat. Commun.* **11**, 3828 (2020).

48. Verma, R. et al. Nickel-laden dendritic plasmonic colloidosomes of black gold: forced plasmon mediated photocatalytic CO_2 hydrogenation. *ACS Nano* **17**, 4526–4538 (2023).

49. Dhiman, M. et al. Plasmonic colloidosomes of black gold for solar energy harvesting and hotspots directed catalysis for CO_2 to fuel conversion. *Chem. Sci.* **10**, 6594–6603 (2019).

50. Thankamony, A. S. L. et al. Insights into the catalytic activity of nitridated fibrous silica (KCC-1) nanocatalysts from ^{15}N and ^{29}Si NMR spectroscopy enhanced by dynamic nuclear polarization. *Angew. Chem. Int. Ed.* **54**, 2190–2193 (2015).

51. Singh, S. et al. Surface plasmon-enhanced photo-driven CO_2 hydrogenation by hydroxy-terminated nickel nitride nanosheets. *Nat. Commun.* **14**, 2551 (2023).

52. Maarisetty, D. & Baral, S. S. Defect engineering in photocatalysis: formation, chemistry, optoelectronics, and interface studies. *J. Mater. Chem. A* **8**, 18560 (2020).

53. Hong, S. B. & Camblor, M. A. SiO^- defects in as-synthesized pure-silica and aluminosilicate sodalites. *Chem. Mater.* **9**, 1999–2003 (1997).

54. Skuja, L. Section 1. Defect studies in vitreous silica and related materials: Optically active oxygen-deficiency-related centers in amorphous silicon dioxide. *J. Non-Cryst. Solids* **239**, 16–48 (1998).

55. Novatski, A. et al. Relations among nonbridging oxygen, optical properties, optical basicity, and color center formation in CaO–MgO aluminosilicate glasses. *J. Appl. Phys.* **104**, 094910 (2008).

56. Skuja, L. Section 2. Point defects in silica glass: luminescence and optical absorption: the origin of the intrinsic 1.9 eV luminescence band in glassy SiO_2. *J. Non-Cryst. Solids* **179**, 51–69 (1994).

57. Skuja, L., Tanimura, K. & Itoh, N. Correlation between the radiation-induced intrinsic 4.8 eV optical absorption and 1.9 eV photoluminescence bands in glassy SiO_2. *J. Appl. Phys.* **80**, 3518 (1996).

58. Li, S. et al. Extra-framework aluminium species in hydrated faujasite zeolite as investigated by two-dimensional solid-state NMR spectroscopy and theoretical calculations. *Phys. Chem. Chem. Phys.* **12**, 3895–3903 (2010).

59. Gabrienko, A. A. et al. H/D exchange of molecular hydrogen with Brønsted acid sites of Zn- and Ga-modified zeolite BEA. *Phys. Chem. Chem. Phys.* **12**, 5149–5155 (2010).

60. Schroeder, C., Siozios, V., Hunger, M., Hansen, M. R. & Koller, H. Disentangling Brønsted acid sites and hydrogen-bonded silanol groups in high-silica zeolite H-ZSM-5. *J. Phys. Chem. C* **124**, 23380–23386 (2020).

61. Salvia, W. S., Zhao, T. Y., Chatterjee, P., Huang, W. & Perras, F. A. Are the Brønsted acid sites in amorphous silica–alumina bridging? *Chem. Commun.* **59**, 13962–13965 (2023).

62. Zhao, Z. et al. Nature of five-coordinated Al in γ-Al_2O_3 revealed by ultra-high-field solid-state NMR. *ACS Cent. Sci.* **8**, 795–803 (2022).

63. Jiang, Y., Huang, J., Dai, W. & Hunger, M. Solid-state nuclear magnetic resonance investigations of the nature, property, and activity of acid sites on solid catalysts. *Solid State Nucl. Magn. Reson.* **39**, 116–141 (2011).

64. Xu, S. et al. High-field one-dimensional and two-dimensional ^{27}Al magic-angle spinning nuclear magnetic resonance study of θ-, δ-, and γ-Al_2O_3 dominated aluminum oxides: toward understanding the Al Sites in γ-Al_2O_3. *ACS Omega* **6**, 4090–4099 (2021).

65. Trebosc, J., Hu, B., Amoureux, J. P. & Gan, Z. Through-space R^3-HETCOR experiments between spin-1/2 and half-integer quadrupolar nuclei in solid-state NMR. *J. Magn. Reson.* **186**, 220–227 (2007).

66. Venkatesh, A., Hanrahan, M. P. & Rossini, A. J. Proton detection of MAS solid-state NMR spectra of half-integer quadrupolar nuclei. *Solid State Nucl. Magn. Reson.* **84**, 171–181 (2017).

67. Al-Nahari, S., Laurencin, D. & Alonso, B. Solvent-free synthesis of zeolites: new insights into the mechanism and non-mechanochemical route. *Microporous Mesoporous Mater.* **350**, 112445 (2023).

68. Ashbrook, S. E., Davis, Z. H., Morris, R. E. & Rice, C. M. ^{17}O NMR spectroscopy of crystalline microporous materials. *Chem. Sci.* **12**, 5016–5036 (2021).

69. Pugh, S. M., Wright, P. A., Law, D. J., Thompson, N. & Ashbrook, S. E. Facile, Room-temperature ^{17}O enrichment of zeolite frameworks revealed by solid-state NMR spectroscopy. *J. Am. Chem. Soc.* **142**, 900–906 (2020).

70. Chen, K. et al. [17]O Labeling reveals paired active sites in zeolite catalysts. *J. Am. Chem. Soc.* **144**, 16916–16929 (2022).

71. Heard, C. J. et al. Fast room temperature lability of aluminosilicate zeolites. *Nat. Commun.* **10**, 4690 (2019).

72. Frydman, L. & Harwood, J. S. Isotropic spectra of half-integer quadrupolar spins from bidimensional magic-angle spinning NMR. *J. Am. Chem. Soc.* **117**, 5367–5368 (1995).

73. Gan, Z. & Kwak, H. –T. Enhancing MQMAS sensitivity using signals from multiple coherence transfer pathways. *J. Magn. Reson.* **168**, 346–351 (2004).

74. Peng, L., Liu, Y., Kim, N., Readman, J. E. & Grey, C. P. Detection of Brønsted acid sites in zeolite HY with high-field ^{17}O-MAS-NMR techniques. *Nat. Mater.* **4**, 216–219 (2005).

75. Bull, L. M. et al. A high-resolution ^{17}O and ^{29}Si NMR study of zeolite siliceous ferrierite and ab initio calculations of NMR parameters. *J. Am. Chem. Soc.* **122**, 4948–4958 (2000).

76. Todea, M., Vanea, E., Bran, S., Berce, P. & Simon, S. XPS analysis of aluminosilicates microspheres bioactivity tested in vitro. *Appl. Surf. Sci.* **270**, 777–783 (2013).

77. Bhowmik, D. & Karmakar, P. Tailoring and investigation of surface chemical nature of virgin and ion beam modified muscovite mica. *Surf. Interface Anal.* **51**, 1–7 (2019).

78. Song, C., Yu, B., Wang, M. & Qian, L. Rapid and maskless nano-patterning of aluminosilicate glass surface via friction-induced selective etching in HF solution. *RSC Adv.* **5**, 79964 (2015).

79. Liu, Y., Zeng, F., Sun, B., Jia, P. & Graham, I. T. Structural characterizations of aluminosilicates in two types of fly ash samples from Shanxi province, north China. *Minerals* **9**, 358 (2019).

80. Yang, B. et al. Enhanced photocatalytic activity of perovskite $NaNbO_3$ by oxygen vacancy engineering. *Phys. Chem. Chem. Phys.* **21**, 11697 (2019).

81. Jakes, P. & Erdem, E. Finite size effects in ZnO nanoparticles: an electron paramagnetic resonance (EPR) analysis. *Phys. Status Solidi RRL* **5**, 56–58 (2011).

82. Liu, S. et al. Solid surface frustrated Lewis pair constructed on layered AlOOH for hydrogenation reaction. *Nat. Commun.* **13**, 2320 (2022).

83. Chiesa, M., Giamello, E. & Che, M. EPR characterization and reactivity of surface-localized inorganic radicals and radical ions. *Chem. Rev.* **110**, 1320–1347 (2010).

84. Vedrine, J. C., Abou-Kais, A., Massardier, J. & Dalmai-Imelik, G. ESR study of deep-bed calcined NH_4Y and aluminum deficient zeolites. *J. Catal.* **29**, 120–128 (1973).

85. Su, L., Chen, X., Wang, H., Wang, Y. & Lu, Z. Oxygen vacancies promoted heterogeneous catalytic ozonation of atrazine by defective 4A zeolite. *J. Clean. Prod.* **336**, 130376 (2022).

86. Kim, M. H., Kim, S. J., Hong, S. B., Seo, G. & Uh, Y. S. Temperature-programmed desorption study of molecular oxygen adsorbed on MFI-type zeolites. *Korean J. Chem. Eng.* **15**, 566–569 (1998).

87. Kustov, L. M. & Kustova, A. L. IR spectroscopic investigation of internal silanol groups in different zeolites with pentasil structure. *Mendeleev Commun.* **31**, 526–528 (2021).

88. Tamargo, C. E. H.-, Roldan, A. & de Leeuw, N. H. A density functional theory study of the structure of pure-silica and aluminium-substituted MFI nanosheets. *J. Solid State Chem.* **237**, 192–203 (2016).

89. Vanelderen, P. et al. Spectroscopic definition of the copper active sites in mordenite: selective methane oxidation. *J. Am. Chem. Soc.* **137**, 6383–6392 (2015).

90. Motagamwala, A. H. & Dumesic, J. A. Microkinetic modeling: a tool for rational catalyst design. *Chem. Rev.* **121**, 1049–1076 (2021).

91. Robatjazi, H. et al. Plasmon-driven carbon–fluorine (C(sp^3)–F) bond activation with mechanistic insights into hot-carrier-mediated pathways. *Nat. Catal.* **3**, 564–573 (2020).

92. He, Y. et al. Sulfated complex metal oxides solid acids with dual Brønsted-Lewis acidic property for production of 5-ethoxymethylfurfural from biomass-derived carbohydrates. *J. Chem. Eng.* **429**, 132279 (2022).

93. Arefieva, O. D., Pirogovskaya, P. D., Panasenko, A. E. & Zemnukhova, L. A. Acid-base properties of aluminosilicates from rice husk and straw. *SN Appl. Sci.* **2**, 894 (2020).

94. Wu, Y., Zhao, W., Wang, W. & Suia, W. Fabricating binary anti-corrosion structures containing superhydrophobic surfaces and sturdy barrier layers for Al alloys. *RSC Adv.* **6**, 5100 (2016).

95. Yan, B., Liu, S., Chastain, M. L., Yang, S. & Chen, J. A new FTIR method for estimating the firing temperature of ceramic bronze-casting moulds from early China. *Sci. Rep.* **11**, 3316 (2021).

96. Luan, Z. & Fournier, J. A. In situ FTIR spectroscopic investigation of active sites and adsorbate interactions in mesoporous aluminosilicates SBA-15 molecular sieves. *Microporous Mesoporous Mater.* **79**, 235–240 (2005).

97. Abdelrahman, E. A. et al. Facile fabrication of novel analcime/sodium aluminum silicate hydrate and zeolite Y/faujasite meso-porous nanocomposites for efficient removal of Cu(II) and Pb(II) ions from aqueous media. *J. Mater. Res Technol.* **9**, 7900–7914 (2020).

98. Singh, R. et al. Probing the interfaces in nanosilica-supported TiO_2 photocatalysts by solid-state NMR and in situ FTIR. *ChemNanoMat* **4**, 1231–1239 (2018).

99. Kayatürk, N., Usanmaz, A. & Önal, A. M. Polymerization by bis(ethylxanthato)-nickel(II) as an initiator. I. Polymerization of styrene oxide. *J. Mass Spectrom.—Pure Appl. Chem. A* **36**, 115–135 (1999).

100. Harris, R. K., Becker, E. D., De Menezes, S. M. C., Goodfellow, R. & Granger, P. NMR nomenclature. nuclear spin properties and conventions for chemical shifts. *Pure Appl. Chem.* **73**, 1795 (2001).

101. Schnell, I., Lupulescu, A., Hafner, S., Demco, D. E. & Spiess, H. W. Resolution enhancement in multiple-quantum MAS NMR spectroscopy. *J. Magn. Reson.* **133**, 61–69 (1998).

102. Hu, B., Trebosc, J. & Amoureux, J. P. Comparison of several heteronuclear dipolar recoupling NMR methods to be used in MAS HMQC/HSQC. *J. Magn. Reson.* **192**, 112–122 (2008).

103. Brinkmann, A. & Kentgens, A. P. M. Proton-selective [17]O–[1]H distance measurements in fast magic-angle-spinning solid-state NMR spectroscopy for the determination of hydrogen bond lengths. *J. Am. Chem. Soc.* **128**, 14758–14759 (2006).

104. Yao, Z., Kwak, H. T., Sakellariou, D., Emsley, L. & Grandinetti, P. J. Sensitivity enhancement of the central transition NMR signal of quadrupolar nuclei under magic-angle spinning. *Chem. Phys. Lett.* **327**, 85–90 (2000).

105. d'Espinose de Lacaillerie, J. –B., Fretigny, C. & Massiot, D. MAS NMR spectra of quadrupolar nuclei in disordered solids: the Czjzek model. *J. Magn. Reson.* **192**, 244–251 (2008).

106. van Meerten, S. G.-J., Franssen, W. M.-J. & Kentgens, A. P. M. ssNake: a cross-platform open-source NMR data processing and fitting application. *J. Magn. Reson.* **301**, 56–66 (2019).

Acknowledgements

Author contributions

V.P. proposed the research direction, designed the project, and guided the project. V.P. and R.V. designed various experiments. R.V. performed the experiments (synthesis, characterizations, catalysis) assisted by C.S. Data were analyzed by R.V., V.P., and C.S. A.V. designed and carried out solid-state NMR experiments. R.V. A.V., and V.P. analyzed the NMR data and wrote the discussion. R.V. and V.P. wrote the overall manuscript. Everyone commented on the manuscript.

Competing interests

The authors declare no competing interests.

Additional information